Inorganic Chemistry

pubs.acs.org/IC

Article

Effect of Oxygen-Donor Charge on Adjacent Nitrogen-Donor Interactions in Eu^{3+} Complexes of Mixed N,O-Donor Ligands Demonstrated on a 10-Fold $[Eu(TPAMEN)]^{3+}$ Chelate Complex

Kathleen Schnaars,* Masashi Kaneko,* and Kiyoshi Fujisawa

Cite This: *Inorg. Chem.* 2021, 60, 2477−2491

Read Online

ACCESS | Metrics & More | Article Recommendations | Supporting Information

ABSTRACT: To reduce high-level radiotoxic waste generated by nuclear power plants, highly selective separation agents for minor actinides are mandatory. The mixed N,O-donor ligand *N,N,N′,N′*-tetrakis[(6-carboxypyridin-2-yl)methyl]ethylenediamine (H_4TPAEN; **1**) has shown good performance as a masking agent in Am^{3+}/Eu^{3+} separation studies. Adjustments on the pyridyl backbone to raise the hydrophilicity led to a decrease in selectivity and a decrease in $M^{3+}-N^{am}$ interactions. An enhanced basicity of the pyridyl N-donors was given as a cause. In this work, we examine whether a decrease in O-donor basicity can promote the $M^{3+}-N^{am}$ interactions. Therefore, we replace the deprotonated "charged" carboxylic acid groups of $TPAEN^{4-}$ by neutral amide groups and introduce *N,N,N′,N′*-tetrakis[(6-*N″,N‴*-diethylcarbamoylpyridin-2-yl)methyl]ethylenediamine (TPAMEN; **2**) as a new ligand. TPAMEN was crystallized with $Eu(OTf)_3$ and $Eu(NO_3)_3{\cdot}6H_2O$ to form positively charged 1:1 $[Eu(TPAMEN)]^{3+}$ complexes in the solid state. Alterations in the M−O/N bond distances are compared to $[Eu(TPAEN)]^-$ and investigated by DFT calculations to expose the differences in charge/energy density distributions at europium(III) and the donor functionalities of the $TPAEN^{4-}$ and TPAMEN. On the basis of estimations of the bond orders, atomic charges spin populations, and density of states in the Eu and potential Am and Cm complexes, the specific contributions of the donor−metal interaction are analyzed. The prediction of complex formation energy differences for the $[M(TPAEN)]^-$ and $[M(TPAMEN)]^{3+}$ (M^{3+} = Eu^{3+}, Am^{3+}) complexes provide an outlook on the potential performance of TPAMEN in Am^{3+}/Eu^{3+} separation.

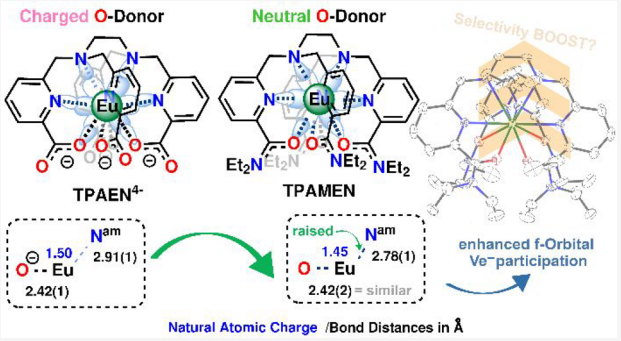

INTRODUCTION

The separation of long-lived radiotoxic minor actinides (MAs: i.e., Am^{3+}, Cm^{3+}) and lanthanides (Ln^{3+}) is crucial for the success of the partitioning and transmutation strategy to reduce the high-level radioactive waste inventory of nuclear power plants in the future.[1,2] Their very similar physicochemical properties still render the separation of MAs and Ln^{3+} challenging. To increase the economics of current separation processes, the development of highly selective separation agents is mandatory. Especially, softer N-donor ligands have proven to have good selectivity toward MAs over Ln^{3+} due to the slight presence of a covalent character in their interaction toward MAs.[3,4] Unfortunately, pure N-donor ligands hardly coordinate the Ln^{3+}/An^{3+} (An^{3+} denotes actinides) ions under highly acidic concentrations as a consequence of concurrent protonation reactions.[3] Mixed N,O-donor ligands overcome this problem by additional oxygen moieties attached to the nitrogen scaffold to increase the ligand's basicity.[5,6]

Less selective harder O-donors counteract the interactions between the Ln^{3+}/An^{3+} ions and the softer N-donors in the same molecule. Bravard et al. demonstrated this by the example of the tripodal ligands tris[(2-pyridyl)methyl]amine (TPA) and tris[6-((2-*N,N*-diethylcarbamoyl)pyridyl)methyl]-amine (TPAAM) (Figure 1), where the $Ln^{3+}-N^{am}$ bond distance for TPAAM was elongated.[7] A comparison with *α,α′,α″*-nitrilotris(6-methyl-2-pyridinecarboxylic acid) (H_3TPAA) (Figure 1) revealed that the $Ln^{3+}-O$ and $Ln^{3+}-N^{py}$ bond distances in these flexible systems are similar independent of the oxygen donor charge.[7] Unfortunately, structural differences and variations in the type of associated anions and solvent molecules, completing the coordination sphere of the Ln^{3+} complexes with TPAAM and H_3TPAA, prevent a direct correlation between the O-donor type (neutral or negatively charged) on the $Ln^{3+}-N^{am}$ bond distances in this study. Whether the observed tendencies in the bond distances

Received: November 18, 2020
Published: January 27, 2021

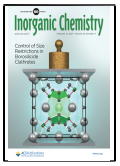

https://dx.doi.org/10.1021/acs.inorgchem.0c03405
Inorg. Chem. 2021, 60, 2477−2491

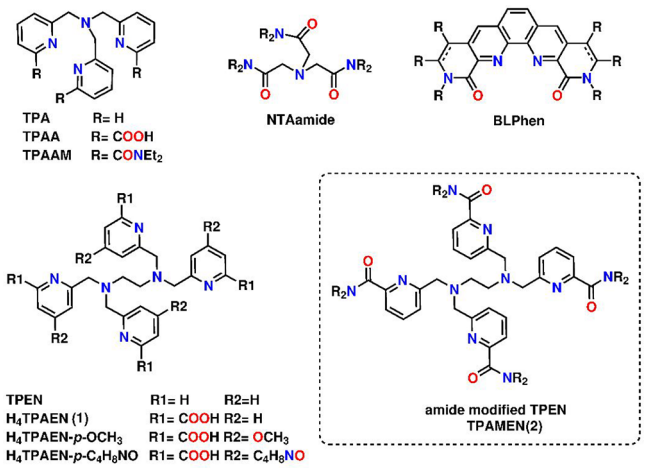

Figure 1. Molecular schemes of TPA, TPAA, TPAAM, NTAamide, BLPhen, TPEN, H_4TPAEN (**1**), H_4TPAEN-*p*-OCH_3, H_4TPAEN-*p*-C_4H_8NO, and TPAMEN (**2**).

are the consequence of steric restrictions or are the result of saturation in charge density at the cation, lowering the metal−ligand attraction, as has been described in quantum mechanistic studies by Berny et al.,[8] remains unclear.

Among the numerous perturbing parameters in the complex coordination systems of f-block elements, including high coordination numbers of between 6 and 12, different coordination geometries, and varying amounts of additional solvent and anion interactions, specific structure-related reactivity changes are hard to identify. Therefore, to enable structure−reactivity correlations, ligands with a high number of available donor functionalities, capable of completely saturating the coordination sphere, are of great interest. Chromophore Ln^{3+} receptors for biomedical applications, which need to be stable under physiological conditions and should avoid additional water coordination to gain higher quantum yields, fulfill this condition. A prominent example is *N,N,N′,N′*-tetrakis[(6-carboxypyridin-2-yl)methyl]ethylenediamine (H_4TPAEN; **1**) (Figure 1), capable of completely encapsulating Ln^{3+} ions by 10-fold coordination.[9] H_4TPAEN is a tetrapodal, decadentate ligand with a 6-fold N-donor framework, based on *N,N,N′,N′*-tetrakis(2-pyridylmethyl)-ethylenediamine (TPEN) (Figure 1), extended by four additional carboxylic acid groups. The TPEN framework also renders this ligand as having promise for selective MA separation, which has initiated several studies on its Am^{3+}/Eu^{3+} and Am^{3+}/Cm^{3+} selectivity.[10,11] Despite its high separation factor for Am^{3+}/Eu^{3+}, H_4TPAEN's poor solubility under acidic conditions limits its application in separation processes and requests further adjustments of the ligand design.[11] The attempts by Gracia et al. to increase the solubility of the ligand in aqueous media by introducing polar groups in the para position of the pyridyl ring resulted in the desired higher solubility but also in a loss of Am^{3+}/Eu^{3+} selectivity.[11]

A quantum chemical study by Huang et al. on the Am^{3+}/Cm^{3+} selectivity of H_4TPAEN (**1**), H_4TPAEN-*p*-OCH_3, and H_4TPAEN-*p*-C_4H_8NO (C_4H_8NO denotes a morpholine group) (Figure 1) pointed out that the An^{3+}−N^{am} bond distances in these ligands correlate with their separation ability for Am^{3+} and Cm^{3+}.[12] An analysis of the electronic structure also suggested an increased charge density at the pyridyl nitrogen in the order H_4TPAEN (**1**) < H_4TPAEN-*p*-OCH_3 < H_4TPAEN-*p*-C_4H_8NO.[12] As a consequence,the An^{3+}−N^{py} bond distance decreases, whereas the An^{3+}−O and the An^{3+}−N^{am} bond distances experience an elongation.[12] The author explains this trend as a steric effect pushing the N^{am} and O away from the actinide.[12] However, this tendency also agrees with the concept of a negative charge-saturated cation with a reduced affinity for further interactions toward other donor atoms in the same molecule as discussed above.[8]

In this study, we intend to promote the M^{3+}−N^{am} interactions by reducing the basicity of adjacent donor functions. To achieve this without tremendously altering the coordination environment, our idea is to replace the cation-exchanging O-donor atoms of H_4TPAEN (**1**) by neutral O-donors of amide groups. The amide group is a popular structural motif in separation agents for f-block elements, such as NTAamide[13] (Figure 1) and BLPhen[14] (Figure 1), because of its high acid stability, relatively hard electron donor character in comparison to other ketones,[15] and good hydrophobic properties due to the possibility of introducing nonpolar alkyl chains at the amide nitrogen.[16] Herein, we report on the decadentate amide-substituted TPEN derivative *N,N,N′,N′*-tetrakis[(6-*N″,N‴*-diethylcarbamoylpyridin-2-yl)-methyl]ethylenediamine (TPAMEN; **2**) (Figure 1). We give two synthetic paths to obtain TPAMEN (**2**) and investigate its complexation behavior toward $Eu(OTf)_3$ and $Eu(NO_3)_3 \cdot 6H_2O$. A comparison of the different molecular structures of both salts serves as an indicator for possible steric influences of the packing, affecting the Eu^{3+}−O/N^{py}/N^{am} bond distances of the complexes in the solid state. DFT calculations of $[Eu(TPAMEN)]^{3+}$ and $[Eu(TPAEN)]^{-}$ estimate how the alterations in the experimental M^{3+}−L bond distances affect the electron-/energy-density properties, the bond order of the present metal−ligand interactions, and the effect of these on the atomic charge and spin population at the cation and each donor functionality. In addition, a prediction of the equivalent Am^{3+} and Cm^{3+} complexes serves as a further validation of the potential effect on actinide complexation and evaluates TPAMEN's potential for selective Am^{3+}/Eu^{3+} separation. With this exemplary investigation of TPAMEN in relation to $TPAEN^{4-}$, we want to determine the complex interplay of donor−metal interactions and their contribution to d- and f-orbital overlap. Moreover, we want to emphasize the importance of shifts in the strength of donor−metal interactions as a result of basicity changing modifications on adjacent donor groups and encourage its consideration in the development of new separation agents in the future.

EXPERIMENTAL SECTION

Materials and Methods. The chemicals used were purchased from Sigma-Aldrich, Merck, Wako, and TCI. CH_2Cl_2, CH_3CN, CH_3OH, and ethylenediamine were predried by storage over activated 3 Å (CH_2Cl_2, CH_3CN, CH_3OH) or 5 Å (ethylenediamine) molecular sieves.[17] If not stated differently, all chemicals were used without further purification. Deionized water was obtained from a Merck Milli-Q reference A^+ water purification system. For path **I**, **1** was synthesized in a five-step synthesis by starting from commercially available 2,6-dipicolinic acid according to a protocol by Gracia et al.[11] The number of associated hydrochlorides and hydrates was determined by elemental analysis. For path **II**, precursor **3** was synthesized in a five-step synthesis (see Scheme S1 in the Supporting Information) by starting from the commercially available 2,6-dipicolinic acid (**4**). The single-step syntheses of compounds, including dimethylpyridine-2,6-picolinate (**5**),[18] 6-

https://dx.doi.org/10.1021/acs.inorgchem.0c03405
Inorg. Chem. 2021, 60, 2477−2491

Table 1. Crystallographic Data for 9 and 10

	[Eu(TPAMEN)][Eu(NO$_3$)$_6$]·2CH$_3$CN·0.45H$_2$O (**9**)	[Eu(TPAMEN)]OTf$_3$·1.125H$_2$O·0.545CH$_3$CH$_2$OH[+solvents] (**10**)
CCDC no.	2018225	2018224
chemic formula	$C_{50}H_{70.9}Eu_2N_{18}O_{22.45}$	$C_{50.09}H_{69.27}EuF_9N_{10}O_{14.67}S_3$
formula wt	1587.26	1465.36
temp (K)	178.0	178.0
cryst syst	orthorhombic	orthorhombic
space group	*Pnna*	*Pbca*
a (Å)	16.3723(3)	15.3371(19)
b (Å)	21.5347(4)	19.232(2)
c (Å)	18.0522(3)	42.232(5)
α (deg)	90	90
β (deg)	90	90
γ (deg)	90	90
V (Å^3)	6364.7(2)	12456.6(3)
Z	4	8
density (g·cm^{-3})	1.656	1.563
F(000)	3210	5993
radiation type	Mo Kα (λ = 0.71073)	Mo Kα (λ = 0.71073)
μ(Mo Kα) (mm^{-1})	2.043	1.204
crystal size (mm)	0.213 × 0.083 × 0.047	0.126 × 0.078 × 0.040
no. of measd rflns	193036	376698
no. of indep rflns	7309	14260
R(int)	0.0565	0.0573
no. of variables	463	958
residuals: $R1$ ($I > 2\sigma(I)$)[a]	0.0477	0.0678
residuals: R (all rflns)	0.0499	0.0736
residuals: $wR2$ ($I > 2\sigma(I)$)[a]	0.0981	0.1534
goodness of fit	1.275	1.297

[a] $R1 = \sum||F_o| - |F_c||/\sum|F_o|$; $wR2 = [\sum(w(F_o^2 - F_c^2)^2)/\sum w(F_o^2)^2]^{1/2}$.

(methoxycarbonyl)picolinic acid (**6**),[18] 6-(*N*,*N*-diethylcarbamoyl)-pyridine-2-carboxylic acid (**7**),[19] *N*,*N*-diethyl(6-(hydroxylmethyl)-pyridine-2-carboxamide (**8**),[7] and *N*,*N*-diethyl(6-chloromethyl)-pyridine-2-carboxamide (**3**),[7] were performed as described in the literature.

FT-IR spectra were measured on a JASCO FT/IR-4600 spectrometer at 2 cm^{-1} spectral resolution. For the measurement, the sample was diluted in CH$_3$CN, transferred to a 3M Type 61 polyethylene 19 mm Aperture IR card, and measured after the evaporation of the solvent. The intensities are reported relative to the peak with the weakest transmission, using the following abbreviations: vw = very weak, w = weak, m = medium, s = strong, vs = very strong.

The ^{1}H NMR were measured at 300.0 K and 500.13 MHz on a Bruker Advance III 500 spectrometer. The ^{13}C{^{1}H} NMR and the Dept-135-NMR spectra were measured at 300.0 K and 100.61 MHz on a Bruker Advance III 400 spectrometer. The chemical shifts (δ) are reported in parts per million (ppm) relative to the residual solvent shifts of CHCl$_3$ in CDCl$_3$ (^{1}H NMR, 7.26 ppm; ^{13}C NMR, 77.16 ppm.[20] Multiplicities are described with s for singlets, d for doublets, t for triplets, q for quadruplets, and m for multiplets. The signals of the ^{13}C{^{1}H} spectra were assigned, supported by Dept-135-NMR spectra. Mass spectrometry was carried out on a Shimadzu LCMS 8030 liquid chromatograph mass spectrometer using electrospray ionization (ESI). CH$_3$CN served as the mobile phase (LC-MS grade). The m/z range was set from 100 to 1000. The samples were directly injected, without any purification over an LC column. The CHN analysis was performed on an Elementar Analysatorsysteme Vario MICRO cube Elemental Analyzer in CHN mode.

Synthesis of *N*,*N*,*N*′,*N*′-Tetrakis[(6-*N*″,*N*″-diethylcarbamoyl-pyridin-2-yl)methyl]ethylenediamine (TPAMEN; 2) via Path I. Thionyl chloride (11.3 mL) and a catalytic amount of DMF (1 drop) were added to *N*,*N*,*N*′,*N*′-tetrakis[(6-carboxypyridin-2-yl)methyl]-ethylenediamine trihydrochloride (H$_4$TPAEN; **1**) (0.849 g, 1.195 mmol) at 0 °C under an argon atmosphere. The reaction mixture was heated to 60 °C and stirred for 1.5 h. During this period the solid gradually dissolved and a yellowish solid spontaneously precipitated. The reaction was stopped, and the excess thionyl chloride was evaporated under reduced pressure. The yellowish solid was redissolved in dry dichloromethane and cooled to 0 °C. Then diethylamine (28.442 mmol, 3 mL) was added dropwise and the reaction mixture was stirred for 2 h at 40 °C. To stop the reaction, an NH$_4$Cl solution was added. The dichloromethane phase was washed 2 times with NH$_4$Cl solution and 2 times with deionized water. The collected organic phases were dried over Na$_2$SO$_4$ and filtered, and the dichloromethane was evaporated, resulting in a yellowish oil. The crude product was purified by column chromatography (neutral Al$_2$O$_3$, 3/2 *n*-hexane/CHCl$_3$ and MeOH gradient from 0% to 10%), yielding 0.699 g of the target compound (L·1.5H$_2$O·HCl: 66%).

IR (FT/IR, 298 K, cm^{-1}): 3547 (vw), 3503 (vw), 3063 (w), 2973 (s), 2935 (s), 2873 (m), 2849 (m), 2821 (m), 1633 (vs), 1587 (vs), 1571 (vs), 1513 (w), 1483 (vs), 1433 (vs), 1416 (s), 1379 (s), 1362 (s), 1348 (m), 1316 (s), 1298 (s), 1269 (m), 1219 (m), 1204 (m), 1154 (m), 1116 (s), 1100 (m), 1084 (s), 1049 (w), 1015 (w), 1011 (w), 994 (m), 978 (w), 945 (w), 906 (vw), 821 (m), 787 (m), 760 (s), 695 (vw), 639 (w), 587 (vw), 505 (vw). ^{1}H NMR (500 MHz, CDCl$_3$, ppm): 1.11 (t, ^3J = 6.9 Hz, 12H, H1), 1.24 (t, ^3J = 7.0 Hz, 12H, H1), 1.96 (s, 2H$_2$O), 2.73 (s, 4H, H10), 3.27 (q, ^3J = 6.9 Hz, 8H, H2), 3.52 (q, ^3J = 7.0 Hz, 8H, 2), 3.76 (s, 8H, H9), 7.39 (d, ^3J = 7.6 Hz, 4H, H5/H7), 7.44 (d, ^3J = 7.8 Hz, 4H, H5/H7), 7.66 (t, ^3J = 7.7 Hz, 4H, H6). ^{13}C{^{1}H} NMR (125 MHz, CDCl$_3$, ppm): 13.0 (4C, C1), 14.4 (4C, C1), 40.3 (4C, C2), 43.4 (4C, C2), 52.7 (2C, C10), 60.7 (4C, C9), 121.4 (4C, C$_{Ar}$), 123.1 (4C, C$_{Ar}$), 137.4 (4C, C$_{Ar}$), 154.5 (4C, C8/C4), 158.7 (4C, C4/C8), 168.7 (4C, C3). LC-MS (m/z): 821.9 [M + H]$^+$, 843.85 [M + Na]$^+$ Anal. Calcd for C$_{46}$H$_{65}$N$_{10}$O$_{4.5}$ [L + 0.5H$_2$O]: C, 66.56; H, 7.89; N, 16.87. Found: C, 66.59; H, 7.63; N, 16.46.

Synthesis of *N*,*N*,*N*′,*N*′-Tetrakis[(6-*N*″,*N*″-diethylcarbamoyl-pyridin-2-yl)methyl]ethylenediamine (TPAMEN; 2) via Path II. 6-(Chloromethyl)-*N*,*N*-diethyl-2-pyridinecarboxamide (1.404 g, 6.192 mmol) and K$_2$CO$_3$ (0.888 g, 6.422 mmol) were diluted in dry

https://dx.doi.org/10.1021/acs.inorgchem.0c03405
Inorg. Chem. 2021, 60, 2477−2491

acetonitrile (20 mL) under an Ar atmosphere before dry ethylenediamine (103 μL, 1.548 mmol) was added. The reaction mixture was refluxed for 11 h and stirred for an additional 84 h at RT. After the reaction was complete, acetonitrile was evaporated and the crude product was dissolved again in dichloromethane (50 mL). After the dichloromethane phase was washed with deionized water (3 × 50 mL), the dichloromethane phase was dried over Na_2SO_4, filtered, and evaporated under reduced pressure to yield the target compound as a pale yellow oil (0.963 g, 1.172 mmol, 70% yield) of the crude product (92% purity). The spectral data are in accordance with those reported for path **I**.

Synthesis of [Eu(TPAMEN)][Eu(NO$_3$)$_6$]·2CH$_3$CN·0.45H$_2$O (9). A 20.7 mg portion of **2** (92%), dissolved in 224 μL of CH_3CN, was added to a solution of 6.7 mg of $Eu(NO_3)_3·6H_2O$ in 249 μL of CH_3CN. The vial containing the reaction mixture, placed into a larger vial, containing a 1/1 diethyl ether/*n*-hexane mixture, and left at room temperature for slow vapor diffusion of the diethyl ether/*n*-hexane mixture. After several weeks, blocklike single crystals slowly grew from the reaction mixture. The isolation of the bulk material was not attempted, and therefore, the yield was not determined.

Synthesis of [Eu(TPAMEN)]OTf$_3$·1.125H$_2$O·0.545CH$_3$CH$_2$OH-[+solvents] (10). A 168 μL portion of a 0.1 M solution of **2** (92%, 30 mg, 0.033 mmol, in 336 μL EtOH) in EtOH was added to 168 μL of a 0.1 M solution of $Eu(OTf)_3$ (10.3 mg, 0.017 mmol, in 168 μL H_2O) in H_2O. The mixture was frozen by external cooling with liquid nitrogen before a layer of diethyl ether was added. The two-layer system was warmed to RT, and after slow diffusion of the diethyl ether into the EtOH/H_2O solution, crystalline plates of **10**, suitable for X-ray crystallography, formed at the phase border. The isolation of bulk material was not attempted, and therefore, the yield was not determined.

X-ray Diffraction Refinements. The crystal data and refinement parameters for [Eu(TPAMEN)][Eu(NO$_3$)$_6$]·2CH$_3$CN·0.45H$_2$O (**9**) and [Eu(TPAMEN)]OTf$_3$·1.125H$_2$O·0.545CH$_3$CH$_2$OH[+solvents] (**10**) are summarized in Table 1. Suitable single crystals were coated in Paratone-N oil and mounted on a Dual-Thickness MicroLoop LD (200 μM) purchased from MiTeGEn and placed in a N_2 gas stream. The diffraction data were measured on a Rigaku XtaLAB P200 diffractometer using Mo Kα (λ = 0.71073 Å) radiation at 178 K for **9** and **10**. Empirical absorption corrections were performed with CrysAlisPRO.[21] All structures were solved by direct methods (SIR2008)[22] using CrystalStructure,[23] and refinement was performed in OLEX2-1.3-alpha[24] with SHELXL[25] by least-squares minimization against F^2. During the refinement, first isotropic and then anisotropic thermal parameters for all non-hydrogen atoms were used. Hydrogen atoms were calculated and placed in idealized positions. Images of the molecular structures were created with OLEX2-1.3-alpha[24,26] and further modified with Gimp.2.10.14.[27] In **9** two of the NEt_2 groups have a disorder of approximately 50%, in which the ethyl residues are flipped around the CH_2 group to open space for disordered water molecules in the packing. Structure **10** shows a high degree of solvent and anion disorder. According to their positioning in the packing the triflate anions are disordered over two and three positions. To fit the triflate molecules on the related residual electron density peaks, the Fragment DB[28,29] extensions of OLEX2-1.3-alpha[24] were used. The high degree of disorder hindered a direct assignment of all solvent molecules in the structure, and a solvent mask was applied. However, the multiple overlaps and vicinities of the residual electron density peaks to the triflate anions led to difficulties with the electron count of the solvent mask. To solve this problem, in a second approach, two triflate anions were squeezed to enable an electron count in the solvent-relevant void. A concise summary of the refinement parameters, the applied constraints and restraints, and a report on the different solvent mask attempts can be found in the Supporting Information. The amount of crystalline solvent was modeled in accordance with the residual electron density peaks. If possible, the occupancy was optimized as a free parameter by the refinement program. In cases where the residual electron density was very low, the occupancy was adjusted by trial under observation of the ORTEP ellipsoids. The amount of solvent is purely defined by the model and may therefore vary from the reality. Due to the high inaccuracy of our model concerning the triflate anions and solvent molecules, the discussion will only focus on global packing properties and selected interatomic metal−ligand distances/angles of the [Eu(TPAMEN)]$^{3+}$ fragment, to which no constraints and restraints had been applied. To enter the responses, corresponding to the alerts in the checkcif files, into the cif files, enCIFer 2020.1[30] was used.

Continuous Shape Measure Calculations (CShM).[31] To determine the shape of the coordination polyhedra of the [Eu(TPAMEN)]$^{3+}$ and [Eu(NO$_3$)$_6$]$^{3-}$ the program SHAPE (2.1)[31] was employed. To create the imput file, the corresponding *xyz* values were extracted from the cif files by using OLEX2-1.3-alpha[24] and Mercury2020.1.[32−36] The closer the value to zero, the higher the agreement to an ideal polyhedral shape.

DFT Calculations. We carried out the geometry optimization, determined the vibrational frequency modes, and carried out single-point energy calculations by using density functional theory (DFT)[37] calculations, followed by electron population analyses, of [M(TPAEN)]$^-$ and [M(TPAMEN)]$^{3+}$ (M^{3+} = Eu^{3+}, Am^{3+}, Cm^{3+}) to compare their coordination bond properties, such as bond lengths and bond orders. The starting coordinates for geometry optimization calculations were referenced to the corresponding single-crystal X-ray diffraction data of [{Eu(TPAEN)}K(H$_2$O)$_3$]·4H$_2$O (CSD code: TAZKEL[9]) and [Eu(TPAMEN)][Eu(NO$_3$)$_6$]·2CH$_3$CN·0.45H$_2$O (**9**) (this study) for [M(TPAEN)]$^-$ and [M(TPAMEN)]$^{3+}$, respectively. We employed a scalar-relativistic zeroth-order regular approximation (ZORA)[38,39] with segmented all-electron relativistically contracted (SARC) basis sets to consider the scalar-relativistic effects of the heavy-metal atoms. The SARC basis sets for ZORA were assigned as {61^{17}/51^{11}/41^8/311} for the Eu atom[40] and (91^{20}/81^{12}/71^9/61^6) to Am and Cm atoms[41] for all DFT calculations and the other atoms as split-valence plus one polarization (SVP)[42] for geometry optimization and vibrational frequency mode calculations and triple-ζ valence plus one polarization (TZVP)[42] for single-point energy calculations. M06-L was used as the exchange-correlation functional[43] for the geometry optimization calculations as well as for thermodynamic analysis in the complex formation reaction. We chose M06-L because it showed good reproduction of the metal−ligand bond lengths of [M(TPAEN)]$^-$ (M^{3+} = Eu^{3+}, Ce^{3+}, Am^{3+}) by benchmarking of density functionals within an optimized time of pure DFT calculations according to a study by Shi et al.[12] Furthermore, the M06-L functional was employed for single-point energy calculations for electron population analyses to enable a comparison of the results of different [M(TPAEN)]$^-$ derivatives by Shi et al.[12] The solvent effect of water was also implicitly considered for all self-consistent-field (SCF) calculations using the conductor-like solvation model (COSMO) method[44] for both geometry optimization and single-point energy calculations. The dielectric constant and refractive index were set to 80.4 and 1.33, respectively, and the COSMO radii were assigned to Eu, Am, Cm, O, N, C, and H atoms as 1.90, 1.99, 1.95, 1.72, 1.83, 2.00, and 1.30 Å, respectively, to consider water solvation effects in the COSMO calculations. We obtained the electronic ground states of [M(TPAEN)]$^-$ and [M(TPAMEN)]$^{3+}$, which were set to a spin septet for M^{3+} = Eu^{3+}, Am^{3+} and a spin octet for M = Cm^{3+}, by using an unrestricted Kohn−Sham treatment to confirm the equilibrium structures to be at a local minimum by vibrational frequency mode calculations. We used the resolution of the identity (RI) approximation[45] for all SCF calculations with the same criteria in the convergence and grid number as in our previous DFT studies.[46] All SCF calculations were performed under a convergence condition, in which the threshold value of total energy change during the iteration was set as 10^{-8} hartree. Grid point parameters were set to a Lebedev194 angular grid with an integral accuracy of 4.34 in geometry optimization and numerical vibrational frequency mode calculations and a Lebedev302 angular grid with an integral accuracy of 4.67 followed by a Lebedev434 final angular grid with an integral accuracy of 5.01 in single-point energy calculations, in which special grids were assigned to Eu^{3+} with an integral accuracy of 14. All DFT calculations and natural population analyses were performed by using ORCA ver. 3.0[47] and NBO ver. 6.0[48] programs, respectively.

https://dx.doi.org/10.1021/acs.inorgchem.0c03405
Inorg. Chem. 2021, 60, 2477−2491

Scheme 1. Synthesis of TPAMEN (2) by Paths I and II[a]

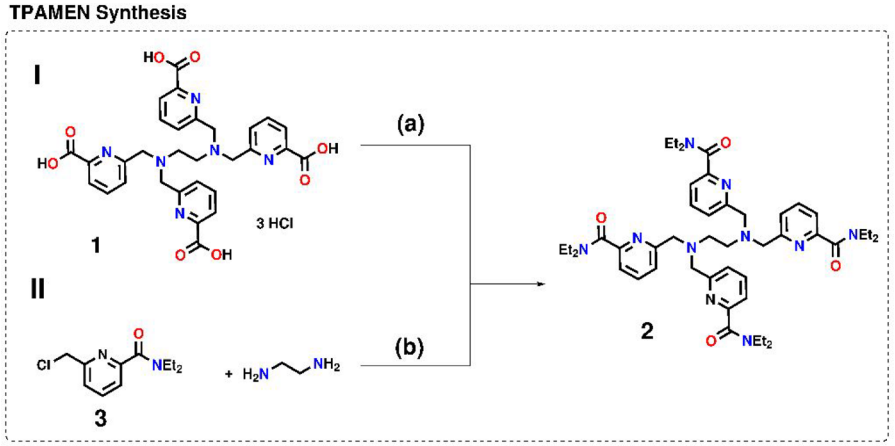

[a]Reagents and conditions: (a) (1) $SOCl_2$, DMF (cat.), 0−60 °C, (2) Et_2NH, CH_2Cl_2, 0−40 °C (66%); (b) K_2CO_3, CH_3CN, reflux, 11 h (70%).

RESULTS AND DISCUSSION

Ligand Synthesis. For the synthesis of TPAMEN (**2**) two different reaction paths were considered (see Scheme 1): (**I**) a direct amide conversion of the carboxyl groups in H_4TPAEN and (**II**) the construction of the TPEN framework on the basis of a 6-(chloromethyl)-2-pyridine carboxamide derivative, already containing the amide moiety. The starting material H_4TPAEN (**1**) for reaction **I** was synthesized by a procedure reported by Gracia et al.[11] The amide conversion was achieved by chlorination of the carboxylic acid groups in **1** with an excess of $SOCl_2$, followed by a subsequent reaction of the acid chloride with diethylamine to give the product **2**. The reaction conditions were chosen on the basis of a procedure by Mariani, Casnati, et al. for the amide conversion of monomethyl dipicolinate (see also Scheme S1c in the Supporting Information).[19] Depending on the prior purification procedure, H_4TPAEN can be obtained with varying amounts of hydrochlorides and hydrates. To ensure complete conversion of all four carboxylic acid groups independent of the number of associated hydrates and hydrochloride, a ≥5 times excess of diethylamine based on the molar mass of pure H_4TPAEN was employed. The reaction gave the isolated TPAMEN (**2**) in fairly good yield (66%).

In reaction **II**, precursor **3** was reacted with ethylenediamine in the presence of K_2CO_3 to assemble the TPEN framework. Also, the second reaction gave **2** in good yield (70%). The starting compound **3** was obtained from 2,6-pyridinedicarboxylic acid in a five-step synthesis in accordance with different literature protocols (see Scheme S1 in the Supporting Information).[7,18,19]

Structural Characterization of Eu^{3+}-TPAMEN Complexes in the Solid State. TPAMEN (**2**) was reacted with $Eu(OTf)_3$ and $Eu(NO_3)_3{\cdot}6H_2O$ to obtain single crystals for structural investigations of the Eu^{3+}-TPAMEN complexation. The attempts to obtain crystals from the reaction of TPAMEN with $Eu(NO_3)_3{\cdot}6H_2O$ resulted primarily in the precipitation of an oily residue containing the complex species. Only once was it possible to grow a blocklike single crystal of $[Eu(TPAMEN)][Eu(NO_3)_6]{\cdot}2CH_3CN{\cdot}0.45H_2O$ (**9**) by vapor diffusion of *n*-hexane/diethyl ether into a saturated solution of the reactants in acetonitrile. Several attempts to reproduce the complexation under the same as well as slightly altered stoichiometric, temperature, and solvent conditions failed. We assume that in the first trial by serendipity a crystal seed formed from the oily residue and gave this one square blocklike crystal, whereas in the other trials this was not achieved. There seems to be a thin window of parameters depending on external temperature and the ratio of acetonitrile/diethyl ether and *n*-hexane where the complex stays soluble and does not form a third layer. We suspect that temperature fluctuations in our laboratory may have hindered the crystal formation in the further trials. The reaction with $Eu(OTf)_3$ readily formed a crystalline solid upon the slow addition of diethyl ether to a solution of TPAMEN and $Eu(OTf)_3$ in methanol, acetonitrile, or ethanol/water. Only the last solvent provided suitable single crystals of $[Eu(TPAMEN)]OTf_3{\cdot}1.125H_2O{\cdot}0.545CH_3CH_2OH$[+solvents] (**10**) for X-ray crystallographic studies.

Crystal data of **9** and **10** are given in Table 1. Selected bond distances of the Eu^{3+} coordination environment for $[Eu(TPAMEN)]^{3+}$ are summarized in Table 2 and for $[Eu(NO_3)_6]^{3-}$ in Table 3. A selection of angles and torsion angles of the $[Eu(TPAMEN)]^{3+}$ fragments in **9** and **10** is summarized in Table S3 in the Supporting Information. Both complexes crystallize in primitive orthorhombic space groups: **9** in *Pnna*

Table 2. Selected Bond Distances (Å) for $[Eu(TPAMEN)]^{3+}$ in $[Eu(TPAMEN)][Eu(NO_3)_6]{\cdot}2CH_3CN{\cdot}0.45H_2O$ (**9**) and $[Eu(TPAMEN)]OTf_3{\cdot}1.125H_2O{\cdot}0.545CH_3CH_2OH$[+solvents] (**10**)

9		10	
		$Eu^{3+}-O$	
Eu1−O1	2.437(3)	Eu1−O1	2.416(4)
Eu1−O2	2.397(3)	Eu1−O2	2.457(4)
		Eu1−O3	2.418(4)
		Eu1−O4	2.436(4)
		$Eu^{3+}-N^{am}$	
Eu1−N1	2.786(4)	Eu1−N1	2.782(5)
		Eu1−N6	2.784(5)
		$Eu^{3+}-N^{py}$	
Eu1−N2	2.734(4)	Eu1−N2	2.605(5)
Eu1−N4	2.599(4)	Eu1−N4	2.710(5)
		Eu1−N7	2.600(5)
		Eu1−N9	2.699(5)

https://dx.doi.org/10.1021/acs.inorgchem.0c03405
Inorg. Chem. 2021, 60, 2477−2491

Table 3. Selected Bond Distances (Å) and Angles (deg) for $[Eu(NO_3)_6]^{3-}$ in $[Eu(TPAMEN)][Eu(NO_3)_6]\cdot 2CH_3CN\cdot 0.45H_2O$ (9)

$Eu^{3+}-O^{NO3}$					
Eu2−O3	2.573(4)	Eu2−O6	2.562(4)	Eu2−O9	2.577(4)
Eu2−O4	2.577(4)	Eu2−O7	2.538(4)	Eu2−O10	2.603(4)
$O^{NO3}-Eu^{3+}-O^{NO3}$					
O3−Eu2−O4	49.63(12)	O3−Eu2−O9′[a]	176.45(14)	O6−Eu2−O6′[a]	177.75(19)
O6−Eu2−O7	49.88(13)	O4−Eu2−O4′[a]	159.26(16)	O7−Eu2−O10	163.59(13)
O9−Eu2−O10	48.86(14)	O4−Eu2−O10′[a]	124.07(13)	O9−Eu2−O4′[a]	132.39(13)
$N^{NO3}\cdots Eu^{3+}\cdots N^{NO3}$					
N6···Eu2···N6′[a]	111.77(17)	N7···Eu2···N7′[a]	151.50(19)	N8···Eu2···N8′[a]	72.70(20)
N6···Eu2···N7′[a]	89.77(13)	N6···Eu2···N8′[a]	148.43(16)	N7···Eu2···N8′[a]	87.08(15)

[a] $x + 1/2, y, z$.

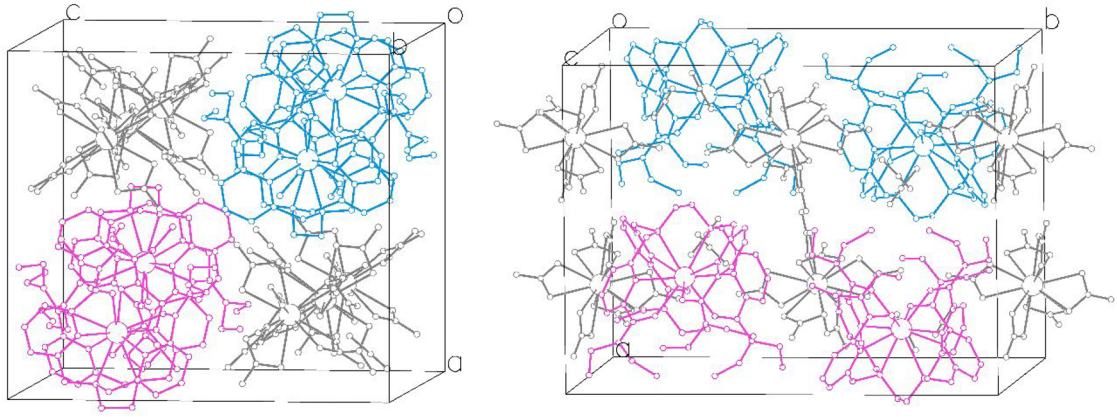

Figure 2. Stereoscopic view along the *b* (left) and *c* (right) axes of the crystal packing in $[Eu(TPAMEN)][Eu(NO_3)_6]\cdot 2CH_3CN\cdot 0.45H_2O$ (**9**). Molecules are displayed as ball and stick diagrams, Eu^{3+} atoms are emphasized with larger spheres, $[Eu(TPAMEN)]^{3+}$ molecules are colored in accordance with their enantiomeric form (blue, Λ; magenta, Δ), and hydrogen atoms have been omitted for clarity.

($P2/n2_1/n2/a$) and **10** in the higher symmetric space group *Pbca* ($P2_1/b2_1/c2_1/a$).

The asymmetric unit of **9** consists of two crystallographic independent half-molecules of $[Eu(TPAMEN)]^{3+}$ and $[Eu(NO_3)_6]^{3-}$, one uncoordinated H_2O molecule with 0.225 occupation, and one free acetonitrile. The Eu^{3+} ions in $[Eu(NO_3)_6]^{3-}$ and $[Eu(TPAMEN)]^{3+}$ occupy special positions of symmetry elements in the unit cell. The Eu^{3+} ion in $[Eu(TPAMEN)]^{3+}$ sits on a 2-fold rotational axis along the direction ($2x$, 1/4, 1/4), which generates the second half of the molecule (x, $y + 1/2$, $z + 1/2$). It also lies on the diagonal (*a*,*c*) glide plane *n* ((1/2, 0, 1/2)x, 1/4, z), which affords the generation of the opposite enantiomer (the asymmetric unit displays the Λ isomer, and the Δ isomer is generated by this symmetry operation). The enantiomeric forms result from the helical arrangement of the picolyl amide arms of TPAMEN encapsulating the Eu^{3+} ion. Likewise, the $[Eu(NO_3)_6]^{3-}$ molecule is completed by a rotation around the 2-fold rotational axis passing through the Eu^{3+} center along the *c* direction (2 1/4, 0, z). A view along the *b* direction [010] (see Figure 2, left) reveals that $[Eu(NO_3)_6]^{3-}$ and $[Eu(TPAMEN)]^{3+}$ form spatially separated and enantiomerically pure strings around the 2-fold screw axis in the *b* direction. Thereby the opposite enantiomers alternate diagonally along the (*a*,*c*) plane. The crystal water takes the cavity around $[Eu(TPAMEN)]^{3+}$ close to the ethyl amide groups and to according its presence (occupancy 0.225), the ethyl group takes two different orientations. The acetonitrile molecules align around $[Eu(NO_3)_6]^{3-}$ along the (*a*,*c*) room diagonal and parallel (1/4 offset) to the vertical (*a*,*c*) diagonal passing through the 0 point. Furthermore, a view along *c* [001] (Figure 2, right) shows that $[Eu(TPAMEN)]^{3+}$ enantiomers (diagonally) aligned at the same (*a*,*c*) glide plane have the also same orientation (e.g., all ethylene bridges point downward). Their orientation is reversed at the adjacent glide plane. Two layers of (*a*,*c*) glide planes sandwich a layer of $[Eu(NO_3)_6]^{3-}$ (hexanitrato) anions, leading to a dense packing of the different complex molecules in the unit cell. With a multiplicity of 8, the unit cell contains 4 $[Eu(NO_3)_6]^{3-}$, $[Eu(TPAMEN)]^{3+}$, 8 0.225 occupied water, and 8 acetonitrile molecules.

Figure 3 shows the asymmetric unit of **10**. It consists of one independent $[Eu(TPAMEN)]^{3+}$ molecule, three noncoordinated triflate anions, one of which shows a disorder (S2A/S2B) over two positions and one has a more severe disorder over three positions (S3A/S3B/S3C), a 1.0 (O14) and a 0.125 (O16) occupied crystal water and one 0.55 occupied ethanol molecule (O15). There are further electron density peaks in the vicinity of the triflate anions (see Q1 and Q2 Figure 3) S1 and S2A/S2B and $[Eu(TPAMEN)]^{3+}$, which could not be assigned to certain solvent molecules (further information is summarized in the Supporting Information). Unlike the case for **9**, the Eu^{3+} of $[Eu(TPAMEN)]^{3+}$ in **10** is not placed on a symmetry operation. Only the "highly disordered triflate" (S3A/S3B/S3C) overlaps with the 2_1 screw axis along *a*, and the hydrogen-bonded water molecules lie on the axial (*a*,*b*) glide plane (in the *a* direction). The large ORTEP ellipsoids indicate the broad thermal deflection of the atoms. In addition,

https://dx.doi.org/10.1021/acs.inorgchem.0c03405
Inorg. Chem. 2021, 60, 2477−2491

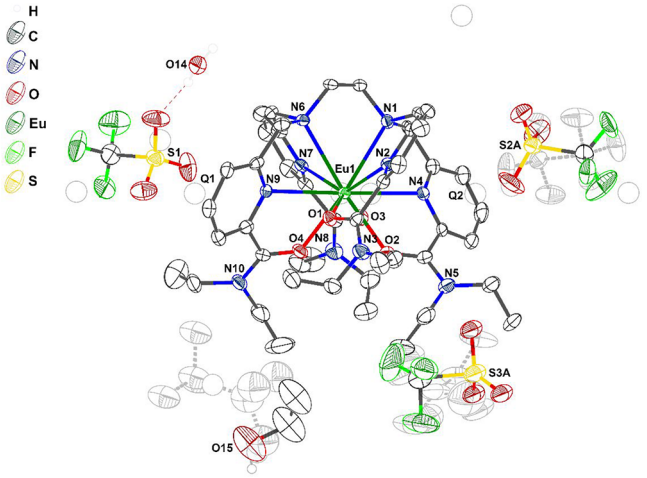

Figure 3. ORTEP diagram of the asymmetric unit of [Eu(TPAMEN)]OTf_3·1.125H_2O·0.545CH_3CH_2OH[+solvents] (**10**) with numeration of selected heteroatoms. thermal ellipsoids are shown at the 50% probability level, and hydrogen atoms attached to carbon have been omitted for clarity.

10 displays a racemic mixture of Δ and Λ isomers of $[Eu(TPAMEN)]^{3+}$ (see Figure 4). The opposite isomer is obtained through reflection at a glide plane.

With the same multiplicity of 8, but the absence of a symmetry element on the $[Eu(TPAMEN)]^{3+}$ molecule as in **10**, the unit cell of **9** contains 8 times [Eu(TPAMEN)]OTf_3·1.125H_2O·0.545CH_3CH_2OH[+solvents] molecules and therefore, has about twice the dimension of the unit cell in **9**. The four layers of alternately oriented (head to head/tail to tail, where the ethylene bridge is defined as the head and the diethylamide groups as the tails) $[Eu(TPAMEN)]^{3+}$ molecules lead to an elongated *c* axis (42.232(5) Å), as is shown in Figure 4. The $[Eu(TPAMEN)]^{3+}$ molecules have ordered layers parallel to the axial glide planes (*a*,*b*) in the direction of *a* (view [010]) and the 2-fold screw axis along *b*. The space between those layers is occupied by alternating layers of triflate S3, filling the space between the tail to tail oriented $[Eu(TPAMEN)]^{3+}$ molecules, and H_2O molecules, occupying the cavities between the head to head oriented $[Eu(TPAMEN)]^{3+}$ molecules. We suspect that due to the large cavity between the tail to tail oriented $[Eu(TPAMEN)]^{3+}$ molecules the degree of freedom in the orientation of triflate ion (S3) is increased, causing its severe degree of disorder. The two residual triflate anions align in the same layer as the $[Eu(TPAMEN)]^{3+}$ molecules.

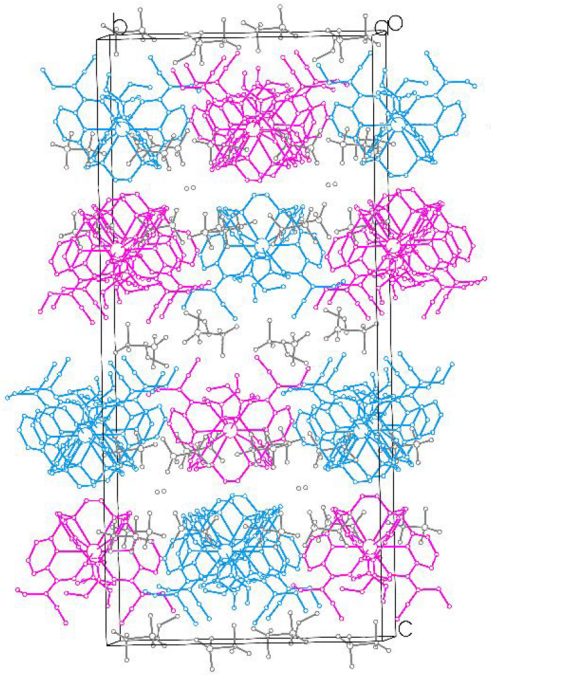

Figure 4. Stereoscopic view of the crystal packing in [Eu(TPAMEN)]OTf_3·1.125H_2O·0.545CH_3CH_2OH[+solvents] (**10**). Molecules are displayed as ball and stick diagrams, Eu^{3+} atoms are emphasized with larger spheres, $[Eu(TPAMEN)]^{3+}$ molecules are colored in accordance with their enantiomeric form (blue, Λ; magenta, Δ), and hydrogen atoms have been omitted for clarity.

Despite the differences in counterions and in packing, the $[Eu(TPAMEN)]^{3+}$ cations in both complexes are very similar (see Figure 3 and Figure 5, left). Eu^{3+} is 10-fold coordinated by

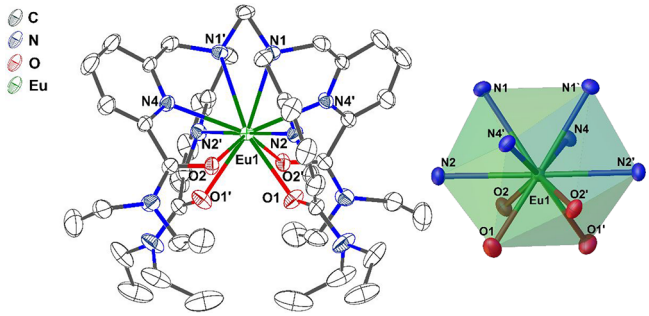

Figure 5. ORTEP diagram of the C_2-symmetric $[Eu(TPAMEN)]^{3+}$ fragment in [Eu(TPAMEN)][$Eu(NO_3)_6$]·2CH_3CN·0.45H_2O (**9**) (left) (thermal ellipsoids are at the 50% probability level and hydrogens have been omitted for clarity) and complex polyhedron (right).

the N_6O_4 donor set of TPAMEN, including the two apical amine nitrogens N^{am}, the four pyridyl nitrogens N^{py}, and the four amide oxygens O. Continuous shape measure (CShM)[31] calculations show that the formed complex polyhedron most resembles a tetradecahedron (TD-10: 2.83 for **9** and 3.02 for **10**) but is also very similar to a staggered dodecahedron (SDD-10: 2.89 for **9** and 3.52 for **10**). The second polyhedron shows a higher agreement with the coordination polyhedron of $[Eu(TPAEN)]^-$[9] (TD-10, 2.85; SDD, 2.48). There are some variations in the orientation of the ethyl substituents at the amide groups of TPAMEN in both complexes. The angles in the $[Eu(TPAMEN)]^{3+}$ molecules are largely congruent (see Table S3). Only the N^{am}–Eu^{3+}–O angles and the N^{py}–C–C–O dihedral angles differ by up to 5 and 9°, respectively. However, the mean Eu^{3+}–donor bond distances (Eu^{3+}–O_{ave}, 2.42(3) Å for **9** and 2.43(2) Å for **10**; Eu^{3+}–N^{py}_{ave} 2.67(10) Å for **9** and 2.65(6) Å for **10**; Eu^{3+}–N^{am}_{ave}, 2.79(1) Å for **9** and 2.78(1) Å for **10**), in accordance with Table 2, are consistent in both complexes. Therefore, we suspect that the different packing environments and the varying angles of the complexes discussed herein have a minor effect on the bond distances in $[Eu(TPAMEN)]^{3+}$ molecules. The comparably large esds for the Eu^{3+}–N^{py}_{ave} result from the unequal alignment of the picolyl amide arms, where two picolyl amide arms in line with the ethylenediamine bridge have longer bond distances (2.73(1) Å for **9**; 2.70(1) Å for **10**) and the two vertically

https://dx.doi.org/10.1021/acs.inorgchem.0c03405
Inorg. Chem. 2021, 60, 2477–2491

aligned picolyl amide arms shorter $Eu^{3+}-N^{py}$ bond distances (2.60(1) Å for **9**; 2.60(1) Å for **10**).

In comparison to $[Eu(TPAEN)]^-$ ($Eu^{3+}-O$ 2.42(1) Å, $Eu^{3+}-N^{py}_{ave}$ 2.65(4) Å, $Eu^{3+}-N^{am}_{ave}$ 2.91(1) Å),[9] the mean $Eu^{3+}-O$ and $Eu^{3+}-N^{py}$ bond distances are on the order of the standard deviation (3σ), whereas the $Eu^{3+}-N^{am}_{ave}$ bond distances in the $[Eu(TPAMEN)]^{3+}$ fragments are significantly shorter by 0.13 Å. The similar $Eu^{3+}-O$ bond distances in $[Eu(TPAEN)]^-$ and $[Eu(TPAMEN)]^{3+}$ show that the difference in charge has only a minor effect on the strength of the $Eu^{3+}-O$ interactions. Similar observations have been reported for $Ln^{3+}-O$ bond distances of the tripodal analogues H_3TPAA and TPAAM, varying between 0 and 5 Å (La^{3+} > Nd^{3+} > Lu^{3+}).[7] It is also conceivable that the additional coordination of K^+ in in $[\{Eu(TPAEN)\}K(H_2O)_3]$ weakens the $Eu^{3+}-O$ interaction.[9] However, there is no significant difference in the $Eu^{3+}-O$ bond distances of the oxygen atoms involved in the K^+ coordination and the that solely bound to Eu^{3+}, opposing this consideration.[9] The mean value of the $Eu^{3+}-N^{am}$ bond distances at 2.78(1) Å is notably shortened by 0.13 Å in comparison to that of $[Eu(TPAEN)]^-$, pointing to an enhanced $M^{3+}-N^{am}$ interaction. Furthermore, the approximately 3 and 11° enhanced mean $N^{py}-Eu^{3+}-N^{py}$ angles of the opposite lying picolyl amide arms at 179(1)° (almost 180°) and 139(1)° in comparison to $[Eu(TPAEN)]^-$ (176 and 128°),[9] respectively, indicate that the Eu^{3+} ion moves closer to the center of the cavity by the 10 donor atoms of TPAMEN. A comparison of the dihedral angles discloses a significant widening of the $N^{py}-C-C-O$ angles (up to |32°|), showing that the amide carbonyl in contrast to the carboxylate group does not have a coplanar alignment to the pyridyl ring. Only the carboxylate substituent not coordinated to K^+ in $[\{Eu(TPAEN)\}K(H_2O)_3]$ shows a higher deviation from the planar alignment by 15°. Therefore, the K^+ coordination may make a notable contribution to the orientation of the carboxylate group.

Figure 6 displays the anionic hexakis(nitrato)europate(III) species $[Eu(NO_3)_6]^{3-}$ present in **9**. Hexakis(nitrato) anions commonly cocrystallize from reactions of neutral ligands, for example, multidentate macrocycles or TEDGA,[49,50] and the corresponding nitrate salt of the lighter up to medium lanthanides. The Eu^{3+} ion in $[Eu(NO_3)_6]^{3-}$ is 12-fold coordinated by six bidentate nitrate ligands, giving an icosahedral coordination polyhedron (CShM IC-12: 1.81)[31] of the oxygen donors. According to CShM calculation (OCT, 7.08; TP, 3.35)[31] the arrangement of the six nitrate N^{NO3} atoms is closest to a slightly distorted trigonal prism, as indicated by the green plains in Figure 6. The $Eu^{3+}-O^{NO3}$ bond distances vary between 2.537(4) and 2.603(4) Å (see Table 3), and the mean inner $O^{NO3}-Eu^{3+}-O^{NO3}$ angle of the bidentate nitrate coordination of 49(1)° is consistent with those observed for other hexakis(nitrato)europate(III) species.[49,50]

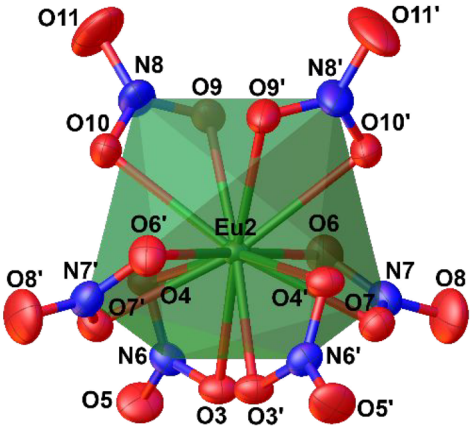

Figure 6. ORTEP diagram of C_2-symmetric $[Eu(NO_3)_6]^{3-}$ in $[Eu(TPAMEN)][Eu(NO_3)_6]\cdot 2CH_3CN\cdot 0.45H_2O$ (**9**) with integrated complex polyhedra (thermal ellipsoids are shown at the 50% probability level).

Molecular Geometry Optimization. Figure 7 displays the optimized geometries of $[Eu(TPAEN)]^-$ and $[Eu(TPAMEN)]^{3+}$ and the corresponding Am^{3+} and Cm^{3+} complexes in aqueous solution using M06-L. Estimated bond lengths between Eu^{3+}, Am^{3+}, and Cm^{3+} and the donor atoms of $TPAEN^{4-}$ and TPAMEN are summarized in Table 4. We added the Am^{3+}/Cm^{3+} geometry optimizations to the discussion to provide an outlook on how the introduction of neutral oxygen donors in TPAMEN changes its reactivity toward actinides in relation to $TPAEN^{4-}$.

All six optimized geometries (see Figure 7) show the metal ions coordinated by the N_6O_4 donor set of the ligands. The calculated geometries reproduce the shorter $Eu^{3+}-N^{am}$ bond length of $[Eu(TPAMEN)]^{3+}$ in comparison to that of $[Eu(TPAEN)]^-$. Accordingly, the Eu^{3+} ion of $[Eu(TPAMEN)]^{3+}$ moves closer to the center of the cavity by the donor atoms, as displayed in Figure 7. The difference in the $Eu^{3+}-N^{am}$ bond lengths of 0.16 Å is consistent with the experimental difference. The calculated $Eu^{3+}-N^{py}$ bond lengths are overestimated by ~0.1 Å in comparison to the experimental values for both $[Eu(TPAEN)]^-$ and $[Eu(TPAMEN]^{3+}$. This overestimation is also observed in the DFT benchmarking on the geometry optimization for $[Eu(TPAEN)]^-$ by 0.05–0.11 Å.[12]

The bond lengths of the optimized actinide complexes tend to be shorter in comparison to the Eu^{3+} complexes, except for the $M^{3+}-O_{ave}$ bond lengths, which increase in the order Eu^{3+} < Cm^{3+} < Am^{3+}. Apart from the $M^{3+}-N^{am}_{ave}$ bond lengths of $[Eu(TPAEN)]^-$ and $[Am(TPAEN)]^-$ no significant variations in the bond lengths are observed. The bond lengths of the Am^{3+} and Cm^{3+} complexes with the same ligand are close to equal. On comparison with the experimental data for the $[Am(TPAEN)]^-$ complex, less of a pronounced overestimation for $M^{3+}-N^{py}_{ave}$ and an underestimation for the $M^{3+}-N^{am}_{ave}$ are displayed. In contrast to the theoretical data the $M^{3+}-N^{am}_{ave}$ distances of the experimental data show no significant difference between the Eu^{3+} and Am^{3+} complexes. Comparing both ligands, we observe shorter $M^{3+}-N^{am}_{ave}$ and longer $M^{3+}-O_{ave}$ distances for the complexes $[M(TPAMEN)]^{3+}$ (M^{3+} = Am^{3+}, Cm^{3+}). The plain differences between the bond lengths in the Eu^{3+} and Am^{3+} complexes suggest a higher effect on the TPAEN complexation and, except for the Eu^{3+} complex, the bond distances are shorter for $[M(TPAMEN)]^{3+}$ and also the shorter bond distances for $[M(TPAEN)]^-$ (M^{3+} = Am^{3+}, Cm^{3+}) point to a more stable complex formation with TPAEN.

Bond Critical Point (BCP) Analysis. More insights into the electron, energy density, and interaction character of the formed bonds are given by a bond critical point (BCP) analysis. The electron density ρ_{BCP} (>0.2, open-shell "covalent" interaction; <0.1, closed-shell interaction referring to ionic, van der Waals, or hydrogen bonding) and the Laplacian $\nabla^2\rho_{BCP}$

https://dx.doi.org/10.1021/acs.inorgchem.0c03405
Inorg. Chem. 2021, 60, 2477–2491

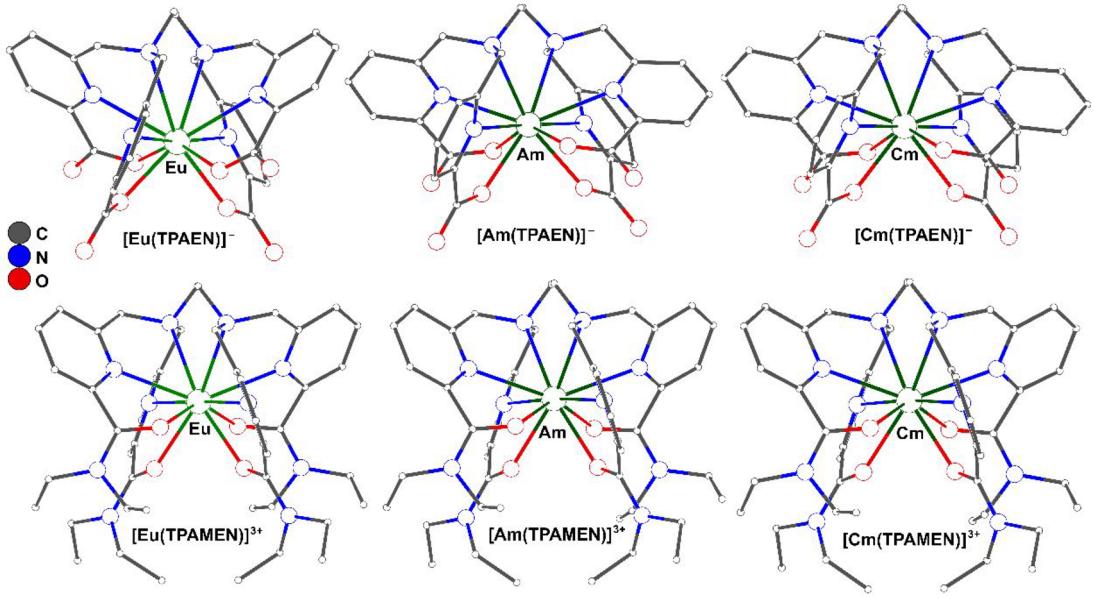

Figure 7. Ball and stick diagrams of the DFT optimized structures of $[M(TPAEN)]^-$ and $[M(TPAMEN)]^{3+}$ (M = Eu, Am, Cm) structures using M06-L.

Table 4. Bond Analysis of the Complexes $[M(TPAEN)]^-$ and $[M(TPAMEN)]^{3+}$ (M^{3+} = Eu^{3+}, Am^{3+}, Cm^{3+})

	bond length (Å)					
	Eu^{3+}		Am^{3+}		Cm^{3+}	
	exptl	calcd	exptl	calcd	exptl	calcd
			$[M(TPAEN)]^-$			
$M^{3+}-N^{am}_{ave}$	2.91(1)[a]	2.951	2.90(2)[c]	2.841(4)		2.841(2)
$M^{3+}-N^{py}_{ave}$	2.65(4)[a]	2.76(2)	2.69(2)[c]	2.72(2)		2.73(5)
$M^{3+}-O_{ave}$	2.42(1)[a]	2.413(6)	2.48(1)[c]	2.46(2)		2.451(7)
			$[M(TPAMEN)]^{3+}$			
$M^{3+}-N^{am}_{ave}$	2.78(1)[b]	2.789		2.736(4)		2.743(5)
$M^{3+}-N^{py}_{ave}$	2.66(6)[b]	2.76(4)		2.75(4)		2.75(5)
$M^{3+}-O_{ave}$	2.42(2)[b]	2.44(2)		2.50(2)		2.48(2)

[a]Reference 9. [b]Average of all corresponding $M^{3+}-O/N$ bond distances determined for **9** and **10** in this work. [c]Reference 51. Values are based on EXAFS.

Table 5. Bond Critical Point (BCP) Analyses of $[M(TPAEN)]^-$ and $[M(TPAMEN)]^{3+}$ (M^{3+} = Eu^{3+}, Am^{3+}, Cm^{3+})

	ρ_{BCP} (e a_0^{-3})			$\nabla^2\rho_{BCP}$ (e a_0^{-5})			$10^{-3}H_{BCP}$		
	Eu^{3+}	Am^{3+}	Cm^{3+}	Eu^{3+}	Am^{3+}	Cm^{3+}	Eu^{3+}	Am^{3+}	Cm^{3+}
				$[M(TPAEN)]^-$					
$M^{3+}-N^{am}_{ave}$	0.0190	0.0275	0.0274	0.0635	0.0881	0.0870	1.26	−0.31	−0.26
$M^{3+}-N^{py}_{ave}$	0.0264	0.0328	0.0327	0.0935	0.1114	0.1113	1.20	−0.35	−0.40
$M^{3+}-O_{ave}$	0.0480	0.0502	0.0502	0.2096	0.2092	0.2137	0.25	−1.62	−1.41
				$[M(TPAMEN)]^{3+}$					
$M^{3+}-N^{am}_{ave}$	0.0270	0.0348	0.0340	0.0872	0.1067	0.1060	0.68	−1.12	−1.12
$M^{3+}-N^{py}_{ave}$	0.0271	0.0320	0.0317	0.0948	0.1064	0.1047	1.04	−0.46	−0.48
$M^{3+}-O_{ave}$	0.0433	0.0443	0.0455	0.1957	0.1901	0.1976	1.31	−0.31	−0.34

(<0, covalent IA/electron density is concentrated in the bond; >0, electron density is diluted from the bond) are values that are necessary to characterize the interaction type between two atoms.[52] In some cases, e.g. electron-rich atoms, where an excessive charge accumulation in the bond area is restricted by the exclusion principle, the aforementioned conditions may not be sufficient to identify a covalent bond.[52] The energy density H_{BCP} is a sufficient condition to describe the covalency of a bond.[52] It is defined by a positive kinetic and a negative potential energy share.[52] When the potential energy part exceeds the kinetic energy part (H_{BCP} < 0), the interaction between the two atoms is defined as covalent; otherwise, a closed-shell interaction is present.

The results of the BCP analysis are summarized in Table 5. For ρ_{BCP} and $\nabla^2\rho_{BCP}$ all values are <0.1 and >0, respectively, pointing to closed-shell interactions. The energy densities H_{BCP}, however, show a different tendency and point to closed-shell interactions of the Eu^{3+} complexes and open-shell interactions in the case of the Am^{3+} and Cm^{3+} complexes. The H_{BCP} values are very small; therefore for the bonding in

https://dx.doi.org/10.1021/acs.inorgchem.0c03405
Inorg. Chem. 2021, 60, 2477−2491

the actinide complexes we suggest slightly covalent interactions. The increase in ρ_{BCP} and $\nabla^2\rho_{BCP}$ is related to the decrease in bond distances (see Table 4). In contrast to the values reported in the literature,[12] the H_{BCP} values of the $M^{3+}-O_{ave}$ interactions in the Am^{3+} and Cm^{3+} complexes both are negative and point to covalent interactions. Also, for $[EuTPAEN)]^-$ H_{BCP} of $M^{3+}-O_{ave}$ displays the least ionic character, which seems to be unusual in a comparison of nitrogen and oxygen donor interactions with lanthanides and may imply back-bonding from the metal. We verified our calculations by reproducing H_{BCP} values of a given optimized structure in the literature (see Table S4 in the Supporting Information), and we suspect that slight differences in the optimized structures are the origin of the present differences. Furthermore, the values obtained for H_{BCP} are very small and may be more prone to fluctuations. The ρ_{BCP} and $\nabla^2\rho_{BCP}$ values are very close and in general show similar tendencies. Except for this, as expected, interactions with shorter bond distances show higher electron densities ρ_{BCP} but also a stronger dilution of charge from the bond due to a higher concentration on the bond. There is also a tendency toward smaller H_{BCP} values for interactions with shorter interatomic distances, pointing to less ionic and more open-shell character of these interactions. Although there is clear enhancement in the nitrogen donor−metal interactions in all $[M(TPAMEN)]^{3+}$ complexes, the summation of all donor−ligand interactions suggests, as a consequence of the significantly smaller H_{BCP} values for all $M^{3+}-O_{ave}$ interactions in $[M(TPAEN)]^-$, that the TPAEN complexes are less ionic and more covalent in character in the case of the actinide complexes. On comparison of the $M^{3+}-O_{ave}$ interactions, the results suggest that the negatively charged carboxylate oxygen provides less of an electrostatic interaction for Eu^{3+} and more of a covalent interaction for Am^{3+} and Cm^{3+}. The neutral amide oxygen in TPAMEN, however, seems to provide interactions with stronger electrostatic character. As a consequence of this, mainly the nature of the $M^{3+}-N^{am}_{ave}$ interactions experiences a shift from more electrostatic character to less electrostatic and more covalent character, which even exceeds that of the $M^{3+}-O_{ave}$ amide interaction.

Mayer Bond Order (MBO). The Mayer bond order analysis[53] provides an overview of all contributions to the bonds. Higher bond orders point to an increased electron population of binding orbitals as well as a reduction or absence of electron population in antibinding orbitals.[54,55] Our results of the MBO analysis of the $[M(TPAEN)]^-$ and $[M(TPAMEN)]^{3+}$ (M^{3+} = Eu^{3+}, Am^{3+}, Cm^{3+}) complexes are summarized in Table 6. With values between 0 and 0.4 we observe weak interactions between the $TPAEN^{4-}$/TPAMEN and the metal cations. The smallest bond orders (0.06−0.11) are displayed for the $M^{3+}-N^{py}_{ave}$ interactions. The difference in oxygen donor charge is reflected by a drop in the $M^{3+}-O_{ave}$ bond orders from ∼0.33 for $[M(TPAEN)]^-$ to ∼0.22 for $[M(TPAMEN)]^{3+}$. Affiliated with changes in bond length, the $M^{3+}-N^{am}_{ave}$ interactions show an opposite trend with bond orders of ∼0.21 and ∼0.34 for the respective complexes with $TPAEN^{4-}$ and TPAMEN. The differences among the three metal complexes of each ligand are rather subtle (<0.05). The actinide complexes show very similar values. Only the higher bond orders for $M^{3+}-O_{ave}$ in $[M(TPAEN)]^-$ and for $M^{3+}-N^{am}_{ave}$ in $[M(TPAMEN)]^{3+}$ point to slightly stronger interactions with the Am^{3+} ion.

Table 6. Mayer Bond Order (MBO) of $[M(TPAEN)]^-$ and $[M(TPAMEN)]^{3+}$ (M^{3+} = Eu^{3+}, Am^{3+}, Cm^{3+})

	Eu^{3+}	Am^{3+}	Cm^{3+}
	$[M(TPAEN)]^-$		
$M^{3+}-N^{am}_{ave}$	0.222	0.202	0.208
$M^{3+}-N^{py}_{ave}$	0.108	0.094	0.093
$M^{3+}-O_{ave}$	0.327	0.333	0.323
	$[M(TPAMEN)]^{3+}$		
$M^{3+}-N^{am}_{ave}$	0.315	0.362	0.335
$M^{3+}-N^{py}_{ave}$	0.103	0.080	0.066
$M^{3+}-O_{ave}$	0.239	0.213	0.214

A closer inspection of the Eu^{3+} and Am^{3+} complex MBOs implies that the donor−metal interactions are not straightforwardly related to the observed bond lengths. For example, in the case of the $M^{3+}-N^{am}_{ave}$ interactions in $[M(TPAEN)]^-$ (M^{3+} = Eu^{3+}, Am^{3+}), a higher population of binding orbitals is detected for $[Eu(TPAEN)]^-$. It is also conspicuous that, despite the similar or even slightly larger $M^{3+}-N^{am}_{ave}$ bond lengths in comparison to $M^{3+}-N^{py}_{ave}$, the bond orders resulting from the N^{am} coordination show higher values in general. Accordingly, we suspect a favorable orbital overlap of binding orbitals and thus their enhanced population in case of the N^{am} donor coordination. Moreover, this suggests a greater effect of the N^{am} donor function on the metal−ligand interaction, which in the case of $[Am(TPAMEN)]^{3+}$ with a bond order of 0.362 even exceeds the strongest carboxylate O^- donor interactions observed for $TPAEN^{4-}$ complexes.

Mulliken Population Analysis (MPA)/Natural Population Analysis (NPA). Table 7 summarizes the atomic charges, spin populations, and electronic configurations of Eu^{3+}, Am^{3+} and Cm^{3+} in $[M(TPAEN)]^-$ and $[M(TPAMEN)]^{3+}$ obtained by MPA[56] and NPA.[57] The alterations of charge and spin population at each single donor function are rather subtle (see Table S5 in the Supporting Information).

The atomic charge q and the excess of the spin populations ρ_{spin} by MPA increase and decrease, respectively, from Eu^{3+} over Am^{3+} to Cm^{3+} for both TPAEN and TPAMEN. Regardless of the metal type the electronic configurations at the d-orbitals remain largely similar and only vary between ∼0.71 in the $[M(TPAEN)]^-$ complexes and ∼0.46 in the $[M(TPAMEN)]^{3+}$ complexes. This variation can likely be attributed to the negative carboxylate oxygens in $TPAEN^{4-}$, providing higher electronic charge to the d-orbitals. However, this variation is not reflected by a drastic difference in the q or ρ_{spin} values for $[M(TPAEN)]^-$ and $[M(TPAMEN)]^{3+}$ of the same cation. The excess of the f-orbital electron configuration, however, decreases from Eu^{3+} over Am^{3+} to Cm^{3+}. On comparison of the complexes $[M(TPAEN)]^-$ and $[M(TPAMEN)]^{3+}$, the f-orbital population in the TPAMEN complexes is slightly enhanced, which is also reflected by a somewhat enhanced spin population of the $[M(TPAMEN)]^{3+}$ complexes.

For the NPA the excess in ρ_{spin} population also decreases in the order Eu^{3+} > Am^{3+} > Cm^{3+}. Herein the actinide complexes exhibit a negative excess (=deficient). This deficiency of spin population may indicate a contribution by the metal ion. The atomic charge populations q of the complexes $[M(TPAMEN)]^{3+}$ increase from Eu^{3+} over Am^{3+} to Cm^{3+}. However, for the complexes $[M(TPAEN)]^-$ a different order, Am^{3+} < Eu^{3+} < Cm^{3+}, is observed. The electronic configuration at the d-orbital is at ∼0.73 for the [M-

https://dx.doi.org/10.1021/acs.inorgchem.0c03405
Inorg. Chem. 2021, 60, 2477−2491

Table 7. Atomic Charge Population, Spin Population, and Electronic Configuration after Mulliken (MPA) and Natural Population Analysis (NPA) of $[M(TPAEN)]^-$ and $[M(TPAMEN)]^{3+}$ (M^{3+} = Eu^{3+}, Am^{3+}, Cm^{3+})

	MPA			NPA		
	q^a	$\rho_{spin}{}^b$	orbital population[c]	q[a]	$\rho_{spin}{}^b$	electronic configuration
			$[M(TPAEN)]^-$			
Eu^{3+}	1.714	6.333	$f^{6.40}d^{0.73}s^{0.09}p^{0.06}$	1.503	6.016	$[Xe]4f^{6.44}5d^{0.69}6s^{0.17}6p^{0.01}$
Am^{3+}	1.862	6.225	$f^{6.31}d^{0.70}s^{0.16}p^{-0.03}$	1.416	5.818	$[Rn]5f^{6.43}6d^{0.76}7s^{0.20}7p^{0.01}$
Cm^{3+}	1.872	7.062	$f^{7.24}d^{0.71}s^{0.18}p^{0.00}$	1.748	6.708	$[Rn]5f^{7.17}6d^{0.75}7s^{0.21}7p^{0.01}$
			$[M(TPAMEN)]^{3+}$			
Eu^{3+}	1.838	6.374	$f^{6.46}d^{0.47}s^{0.10}p^{0.13}$	1.450	6.031	$[Xe]4f^{6.47}5d^{0.63}6s^{0.17}6p^{0.01}$
Am^{3+}	1.994	6.273	$f^{6.35}d^{0.45}s^{0.11}p^{0.09}$	1.519	5.827	$[Rn]5f^{6.43}6d^{0.65}7s^{0.20}7p^{0.01}$
Cm^{3+}	2.058	7.092	$f^{7.28}d^{0.45}s^{0.13}p^{0.09}$	1.842	6.710	$[Rn]5f^{7.16}6d^{0.65}7s^{0.21}7p^{0.01}$

[a]Mulliken/Natural atomic charge. [b]Mulliken/Natural atomic spin population. [c]Without core orbital population.

$(TPAEN)]^-$ complexes similar to the results from an MPA. At ~0.64 the d-orbital electronic configuration in the complexes $[M(TPAMEN)]^{3+}$ are slightly larger in comparison to the MPA. The general trend toward smaller d-orbital population as a consequence of coordination with the neutral oxygen donors in TPAMEN is also reflected by the NPA. The oxygen donor charge seems to have a minor effect on the excess of the f-orbital electronic configuration, which remains consistent for the equivalent complexes of both ligands. A minor enhancement in the f-orbital population (0.03) can be observed for the complex $[Eu(TPAMEN)]^{3+}$. On comparison of all three metal ions, the f-orbital population excess of Cm^{3+} is at ~0.17 significantly lower than that of the other two metal cations (~0.44). A look at the electron configuration distribution at the f- and d-orbitals in combination may offer an explanation for the different trends observed for the atomic charge population q. In $[Am(TPAEN)]^-$ the increased d-orbital population and almost equal f-orbital population may be the reason for the smaller atomic charge population. However, for the $[M(TPAMEN)]^{3+}$ complexes with similar d-orbital populations mainly the variation of the f-orbital electron population leads to the present order.

Density of States (DOS) Analysis. Figure 8 shows the density of states (DOS) diagrams of $[M(TPAEN)]^-$ and $[M(TPAMEN)]^{3+}$. Partial densities of states (PDOSs) of the metal f-orbital electrons are shown as solid lines and overlap population densities of states (OPDOSs) between the metal f-orbitals are shown as dashed lines. The curves are convoluted with a half-width of 0.5 eV. Red and blue dashed lines denote OPDOS curves of $M^{3+}-O_{total}$ and $M^{3+}-N^{am}{}_{total}$ bonds, respectively. The OPDOS curves in the d-orbital DOS diagram display regardless of the metal type exclusively positive distributions for both $M^{3+}(d)-O_{total}$ and $M^{3+}(d)-N^{am}{}_{total}$ bonds, representing bonding-type overlaps. In contrast with that, the f-orbital DOS diagram shows positive OPDOS distributions as well as negative OPDOS distributions, indicating bonding and antibonding-type overlaps. The integral values of OPDOS from the HOMO-29 to the HOMO for the α-spin orbitals in 10^{-2} electron units are also shown in Figure 8. The integral values increase for the $M^{3+}-N^{am}{}_{total}$ bonds and decrease for the $M^{3+}-O_{total}$ bonds from $[M(TPAEN)]^-$ to $[M(TPAMEN)]^{3+}$, reflecting the shift toward stronger $N^{am}-$metal and weaker amide oxygen−metal interactions also observed in the BCP and MBO analyses. The differences between Eu^{3+} and Am^{3+} for all donor−ligand interactions of both ligands suggests that through the dominant increase of the OPDOS of the $Am^{3+}-N^{am}{}_{total}$ bonds a greater distinction between Eu^{3+} and Am^{3+} is obtained in the complexation by

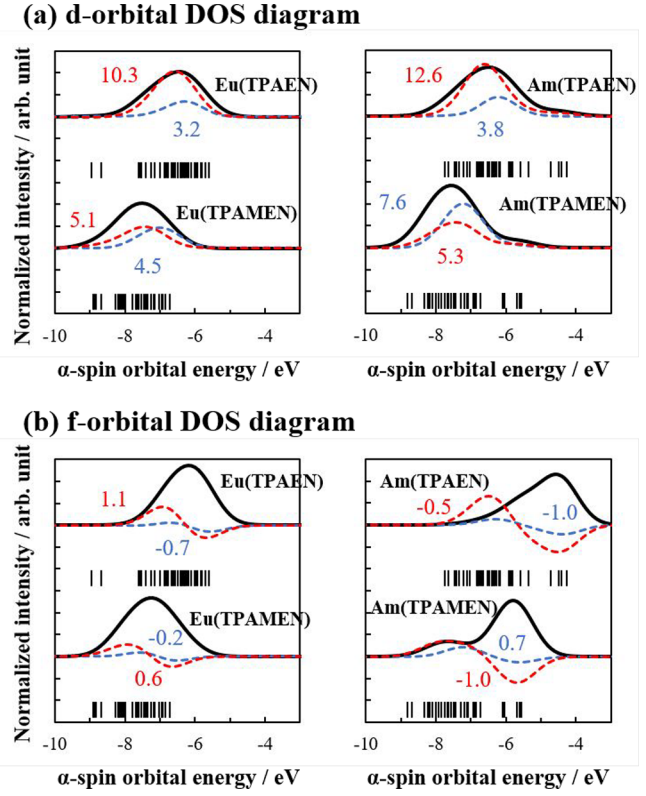

Figure 8. Diagrams of the density of states (DOS) for bonds between metal d- or f-orbitals and donor atoms. Partial DOS curves are presented as black solid lines, and overlap population DOS curves for $M^{3+}-O$ and $M^{3+}-N^{am}$ bonds are displayed as red and blue dashed lines, respectively.

TPAMEN. The DOS values are available inTable S6 in the Supporting Information.

Complex Formation Energies. Gibbs energies were calculated on the basis of the single-point energies and normal vibrational frequencies at the same level as for the geometrical optimization. We estimated the difference in complex formation energies between Eu^{3+} and Am^{3+} on the basis of eq 1 to investigate whether or not Am^{3+}/Eu^{3+} selectivity increases from $TPAEN^{4-}$ to TPAMEN. A negative Gibbs energy difference (ΔG) (see eq 2), on the basis of eq 1, suggests that AmL is more stable than EuL in aqueous solution and also that AmL has a higher complex formation stability. As starting compounds the hydration complexes $[M(H_2O)_9]^{3+}$ and $[M(NO_3)(H_2O)_7]^{2+}$ were considered. Unfortunately, the

https://dx.doi.org/10.1021/acs.inorgchem.0c03405
Inorg. Chem. 2021, 60, 2477−2491

Table 8. Thermodynamic Results for Complexation Reactions Based on Eq 1

reaction	ΔG (kJ mol^{-1}) L = TPAEN^{4-}	ΔG (kJ mol^{-1}) L = TPAMEN	$\Delta\Delta G$ (kJ mol^{-1})	$\Delta\Delta E^{tot}$ (kJ mol^{-1})
n = 0	−3.8	−11.0	−7.2	−8.0
n = 1	−25.0	−32.2		
0.1 M HNO_3	−12.3 [−10.0(10)[a], −12.0(22)[b]]	−19.5		

[a]Experimental value based on a microcalorimetry measurement of [Eu(TPAEN)]$^-$ in ref 10. [b]Experimental value based on time-resolved laser fluorescence spectroscopy of [Eu(TPAEN)]$^-$ in ref 10.

optimization by M06-L failed to converge; therefore, the geometries optimized by the BP86 functional had to be used. The thermal correction to Gibbs energy (G^{corr}) under the standard conditions (see eq 3) was calculated by using quasi-harmonic oscillator and rigid rotator approximations. The calculation details and numerical thermodynamic data are available in Table S7 in the Supporting Information.

$$[EuL] + [Am(NO_3)_n(H_2O)_{9-2n}] \rightarrow [AmL] + [Eu(NO_3)_n(H_2O)_{9-2n}] \quad (1)$$

$$\Delta G(L) = \{G(AmL) + G(Eu(NO_3)_n(H_2O)_{9-2n})\} - \{G(EuL) + G(Am(NO_3)_n(H_2O)_{9-2n})\} \quad (2)$$

$$G = E^{tot} + G^{corr} \quad (3)$$

Table 8 summarizes the thermodynamic data based on eq 1. For both TPAEN^{4-} and TPAMEN the ΔG values are negative. The experimental ΔG value of TPAEN is reported to be −10(1) kJ mol^{-1} in 0.1 M HNO_3 aqueous solution.[51] The ratio between $[M(H_2O)_9]$ and $[M(NO_3)(H_2O)_7]$ in 0.1 M HNO_3 aqueous solution ($C_M < 10^{-4}$ M) at zero ionic strength is estimated to be 53:47 for M^{3+} = Eu^{3+} and 65:35 for M^{3+} = Am^{3+} by using stability constants corrected with the Davies equation:[58] log β = 0.95[59] and 0.74[60] for M^{3+} = Eu^{3+}, Am^{3+}, respectively. The ΔG value of TPAEN is calculated as a weighted sum by a 60:40 ratio for the sake of simplicity to be −12.3 kJ mol^{-1}, being consistent with the experimental value.[51] For TPAMEN the weighted sum of the ΔG values is −19.5 kJ mol^{-1}, which is −7.2 kJ mol^{-1} ($\Delta\Delta G$) lower than that of TPAEN^{4-}. We also computed the $\Delta\Delta G$ values on the basis of the B2PLYP functional,[61] which is known to reproduce Am^{3+}/Eu^{3+} selectivity with various ligands,[46,62] and obtained a difference of −4.3 kJ mol^{-1}. This value suggests that TPAMEN also favors Am^{3+} over Eu^{3+} in the aqueous complex formation reaction and indicates that the stability of its Am^{3+} complex relative to that of its Eu^{3+} complex is higher than that of TPAEN. $\Delta\Delta E^{tot}$ also shows the almost same values of $\Delta\Delta G$ as shown in Table 8, indicating that the lower ΔG value of TPAMEN in comparison to that of TPAEN can be attributed to a difference in inner energy, including ionic and covalent interactions between the metal and L.

$$\Delta\Delta G = \Delta G(TPAMEN) - \Delta G(TPAEN) \quad (4)$$

Deduction of Relation between Metal−Donor (M−D) Bond Parameters and Donor Charge Alterations. By substituting the carboxylate group with an amide group, we reduce the charge at the oxygen and basically lower the energies of the valence orbitals of the molecule.[63] This is also emphasized in Figure 8, where the α-spin orbital energies of the complexes $[M(TPAEN)]^-$ (M^{3+} = Eu^{3+}, Am^{3+}) are higher in comparison to that of the complexes $[M(TPAMEN)]^{3+}$. By lowering the energy of the valence orbitals, we raise the possibility for an interaction with the energetically lower lying f-orbitals. That results likely in a shift in population of bonding and antibonding orbitals, which then in relation to orbital overlap strengthens or weakens the M−D bonding interactions of each donor function, individually. The charge properties of each single donor atom designate the corresponding size and energy level of their valence orbitals and thus their reactivity toward the valence orbitals of the metal cation.[64] The resulting overlap population (OPDOS, MPA, NPA) and the subsequent ratio of bonding and antibonding interactions, which can be described with the bond order (e.g., MBO, Wiberg bond indices) or electron delocalization (δ), then define the bond strengths of each single M−D interaction. All further bond parameters such as equilibrium bond length, charge density ρ_{BCP}, Laplacian $\nabla^2\rho_{BCP}$, and energy density H_{BCP} render descriptive parameters of the chemical bond and arise from the bond strength and in the bonding involved for donor atom types or functional groups as well as steric parameters such as the coordination number.

The alteration of charge (basicity) properties at specific positions affects the energetic level of the ligand molecule orbitals as a whole.[65] Depending on the extent of charge alteration and its distribution in the molecule, this will be more or less pronounced[66] and may result in a switch in order concerning the highest occupied molecular orbital (HOMO). Accordingly, this effect is very sensitive to the composition of the individual ligand system and thus to the energetic compatibility of the donor functions valence orbitals with that of the target metal cation. Therefore, an estimation of this effect without further quantum chemical investigation of the explicit ligand system will likely have only limited precision. Utilizing this interplay in bonding and antibonding interactions by adjusting the HOMO properties of the ligand may be the key to specifically address different unoccupied energetically low lying valence orbitals of certain metal cations to further adjust the selectivity properties. However, this is probably only possible in a very restricted range of energy levels and requires precisely adjusted ligand properties.

CONCLUSION

We introduced TPAMEN, an amide-substituted TPEN derivative, to elucidate the effect of neutral O-donors on the electron distribution around Eu^{3+} and the consequences for the Eu^{3+}−N^{am} interactions. Investigations on the TPAMEN complexation behavior toward $Eu(OTf)_3$ and $Eu(NO_3)_3 \cdot 6H_2O$ yielded mononuclear $[Eu(TPAMEN)]^{3+}$ complexes similar to $[Eu(TPAEN)]^-$. TPAMEN completely encapsulates Eu^{3+} by a 10-fold coordination of 6 N-donor and 4 O-donor atoms. The consistent values for Eu^{3+}−$O/N^{py}/N^{am}$ bond distances regardless of the structural differences in both complexes hint at a negligible effect of the packing on the ligand−metal interactions in the $[Eu(TPAMEN)]^{3+}$ molecule.

https://dx.doi.org/10.1021/acs.inorgchem.0c03405
Inorg. Chem. 2021, 60, 2477−2491

A comparison with $[Eu(TPAEN)]^-$ shows that, despite the difference in O-donor charge, the mean $Eu^{3+}-O$ bond distances in $[Eu(TPAMEN)]^{3+}$ remain similar, whereas the mean $Eu^{3+}-N^{am}$ bond distances are shortened by 0.13 Å. Accompanying changes in the $N^{py}-Eu^{3+}-N^{py}$ angles emphasize that the Eu^{3+} ion moves closer into the center of the 10 donor atoms of TPAMEN. According to the BCP, MBO, and DOS analyses the substitution of the negatively charged oxygen donor with a neutral oxygen causes a significant decrease in covalency and overlap population of bonding orbital $M^{3+}-O_{ave}$ interactions. At the same time the $M^{3+}-N^{am}{}_{ave}$ interactions experience a gain in covalency and OPDOS of the f- and d-orbitals, even surpassing the $M^{3+}-O_{ave}$ amide interactions. We deduced that the charge alteration leads to a shift in the energy levels of valence orbitals by the donor functions, resulting in a redistribution in electron population of bonding and antibonding orbitals, which then determines the bond strength of each single M−D bonding interaction. The eventual effect on TPAMEN separation performance was estimated on the basis of differences in complex formation energies. The results suggest an improved Am^{3+}/Eu^{3+} separation performance for TPAMEN. The same trend is reflected by the difference in integrals of the OPDOSs of the Eu^{3+} and Am^{3+} complexes, where a dominant increase in the $M^{3+}-N^{am}$ OPDOS integral causes a greater distinction between the $[Eu(TPAMEN)]^{3+}$ and $[Am(TPAMEN)]^{3+}$ complexes. In addition, this emphasizes once more the relevance of the $M^{3+}-N^{am}$ interaction for the Am^{3+}/Eu^{3+} selectivity of the ligands. How far these changes in $M^{3+}-N^{am}$ interactions by TPAMEN affects its actual separation ability under experimental conditions will be the subject of future investigations to determine the Am^{3+}/Eu^{3+} separation factors. By demonstrating how subtle changes in O-donor basicity from $[M(TPAEN)]^-$ to $[M(TPAMEN)]^{3+}$ can significantly alter the $M^{3+}-N^{am}$ interactions, we emphasize the relevance of basicity modifications for the strength of adjacent metal−donor interactions. Taking this under consideration, we hope to improve ligand design and selectivity estimations for f-block element receptors in the future.

■ ASSOCIATED CONTENT

Supporting Information

The Supporting Information is available free of charge at https://pubs.acs.org/doi/10.1021/acs.inorgchem.0c03405.

Details of precursor synthesis, NMR data, X-ray crystallography, continuous shape measure files, and DFT calculations (PDF)

Accession Codes

CCDC 2018224−2018226 contain the supplementary crystallographic data for this paper. These data can be obtained free of charge via www.ccdc.cam.ac.uk/data_request/cif, or by emailing data_request@ccdc.cam.ac.uk, or by contacting The Cambridge Crystallographic Data Centre, 12 Union Road, Cambridge CB2 1EZ, UK; fax: +44 1223 336033.

■ AUTHOR INFORMATION

Corresponding Authors

Kathleen Schnaars − *Nuclear Science and Engineering Center, Japan Atomic Energy Agency, Tokaimura, Ibaraki 319−1195, Japan;* orcid.org/0000-0002-6283-9536; Email: schnaars.kathleen@jaea.go.jp

Masashi Kaneko − *Nuclear Science and Engineering Center, Japan Atomic Energy Agency, Tokaimura, Ibaraki 319−1195, Japan;* orcid.org/0000-0001-5428-2144; Email: kaneko.masashi@jaea.go.jp

Author

Kiyoshi Fujisawa − *Department of Chemistry, Ibaraki University, Mito, Ibaraki 310-8512, Japan;* orcid.org/0000-0002-4023-0025

Complete contact information is available at: https://pubs.acs.org/10.1021/acs.inorgchem.0c03405

Author Contributions

The manuscript was written through contributions of all authors. All authors have given approval to the final version of the manuscript. These authors contributed equally.

Notes

The authors declare no competing financial interest.

■ ACKNOWLEDGMENTS

This work was supported by JSPS KAKENHI grant nos. JP16H07439 (M.K.) and JP17K14915 (M.K.) and an Ibaraki University Priority Research Grant (K.F.). We thank Dr. Yuta Kumagai for his support in the laboratory facilities and with the LC/MS measurements. We thank the anonymous reviewers for constructive discussions, adding to the improvement of this manuscript.

■ REFERENCES

(1) Hudson, M. J. Some New Strategies for the Chemical Separation of Actinides and Lanthanides. *Czech. J. Phys.* **2003**, *53* (S1), A305−A311.

(2) Dam, H. H.; Reinhoudt, D. N.; Verboom, W. Multicoordinate Ligands for Actinide/Lanthanide Separations. *Chem. Soc. Rev.* **2007**, *36* (2), 367−377.

(3) Kolarik, Z. Complexation and Separation of Lanthanides(III) and Actinides(III) by Heterocyclic N-Donors in Solutions. *Chem. Rev.* **2008**, *108* (10), 4208−4252.

(4) Neidig, M. L.; Clark, D. L.; Martin, R. L. Covalency in F-Element Complexes. *Coord. Chem. Rev.* **2013**, *257*, 394−406.

(5) Heitzmann, M.; Gateau, C.; Chareyre, L.; Miguirditchian, M.; Charbonnel, M. C.; Delangle, P. Water-Soluble Tetrapodal N,O Ligands Incorporating Soft N-Heterocycles for the Selective Complexation of Am(III) over Ln(III). *New J. Chem.* **2010**, *34* (1), 108−116.

(6) Nash, K. L. A Review of the Basic Chemistry and Recent Developments in Trivalent F-Elements Separations. *Solvent Extr. Ion Exch.* **1993**, *11* (4), 729−768.

(7) Bravard, F.; Bretonnière, Y.; Wietzke, R.; Gateau, C.; Mazzanti, M.; Delangle, P.; Pécaut, J. Solid-State and Solution Properties of Cationic Lanthanide Complexes of a New Neutral Heptadentate N4O3 Tripodal Ligand. *Inorg. Chem.* **2003**, *42* (24), 7978−7989.

(8) Berny, F.; Muzet, N.; Troxler, L.; Dedieu, A.; Wipff, G. Interaction of M^{3+} Lanthanide Cations with Amide, Pyridine, and Phosphoryl O = PPh_3 Ligands: A Quantum Mechanics Study. *Inorg. Chem.* **1999**, *38* (6), 1244−1252.

(9) Chatterton, N.; Bretonnière, Y.; Pécaut, J.; Mazzanti, M. An Efficient Design for the Rigid Assembly of Four Bidentate Chromophores in Water-Stable Highly Luminescent Lanthanide Complexes. *Angew. Chem., Int. Ed.* **2005**, *44* (46), 7595−7598.

(10) Borrini, J.; Favre-Reguillon, A.; Lemaire, M.; Gracia, S.; Arrachart, G.; Bernier, G.; Hérès, X.; Hill, C.; Pellet-Rostaing, S. Water Soluble PDCA Derivatives for Selective Ln(III)/An(III) and Am(III)/Cm(III) Separation. *Solvent Extr. Ion Exch.* **2015**, *33* (3), 224−235.

(11) Gracia, S.; Arrachart, G.; Marie, C.; Chapron, S.; Miguirditchian, M.; Pellet-Rostaing, S. Separation of Am (III) by Solvent Extraction Using Water-Soluble H4tpaen Derivatives. *Tetrahedron* **2015**, *71* (33), 5321−5336.
(12) Huang, P.-W.; Wang, C.-Z.; Wu, Q.-Y.; Lan, J.-H.; Song, G.; Chai, Z.-F.; Shi, W.-Q. Understanding Am^{3+} /Cm^{3+} Separation with H_4TPAEN and Its Hydrophilic Derivatives: A Quantum Chemical Study. *Phys. Chem. Chem. Phys.* **2018**, *20* (20), 14031−14039.
(13) Sasaki, Y.; Tsubata, Y.; Kitatsuji, Y.; Sugo, Y.; Shirasu, N.; Morita, Y.; Kimura, T. Extraction Behavior of Metal Ions by TODGA, DOODA, MIDOA, and NTAamide Extractants from HNO_3 to *n* -Dodecane. *Solvent Extr. Ion Exch.* **2013**, *31* (4), 401−415.
(14) Jansone-Popova, S.; Ivanov, A. S.; Bryantsev, V. S.; Sloop, F. V.; Custelcean, R.; Popovs, I.; Dekarske, M. M.; Moyer, B. A. Bis-Lactam-1,10-Phenanthroline (BLPhen), a New Type of Preorganized Mixed N,O-Donor Ligand That Separates Am(III) over Eu(III) with Exceptionally High Efficiency. *Inorg. Chem.* **2017**, *56* (10), 5911−5917.
(15) Siddall, T. H. Effect of Structure of N,N-Disubstituted Amides on Extraction. *J. Phys. Chem.* **1960**, *64*, 1863−1866.
(16) Baaden, M.; Berny, F.; Madic, C.; Schurhammer, R.; Wipff, G. Theoretical Studies on Lanthanide Cation Extraction by Picolinamides: Ligand-Cation Interactions and Interfacial Behavior. *Solvent Extr. Ion Exch.* **2003**, *21* (2), 199−220.
(17) Williams, D. B. G.; Lawton, M. Drying of Organic Solvents: Quantitative Evaluation of the Efficiency of Several Desiccants. *J. Org. Chem.* **2010**, *75* (24), 8351−8354.
(18) Chen, A. Y.; Thomas, P. W.; Stewart, A. C.; Bergstrom, A.; Cheng, Z.; Miller, C.; Bethel, C. R.; Marshall, S. H.; Credille, C. V.; Riley, C. L.; Page, R. C.; Bonomo, R. A.; Crowder, M. W.; Tierney, D. L.; Fast, W.; Cohen, S. M. Dipicolinic Acid Derivatives as Inhibitors of New Delhi Metallo-β-Lactamase-1. *J. Med. Chem.* **2017**, *60* (17), 7267−7283.
(19) Macerata, E.; Sansone, F.; Baldini, L.; Ugozzoli, F.; Brisach, F.; Haddaoui, J.; Hubscher-Bruder, V.; Arnaud-Neu, F.; Mariani, M.; Ungaro, R.; Casnati, A. Calix[6]Arene-Picolinamide Extractants for Radioactive Waste Treatment: Effect of Additional Carboxy Binding Sites in the Pyridine 6-Positions on Complexation, Extraction Efficiency and An/Ln Separation. *Eur. J. Org. Chem.* **2010**, *2010* (14), 2675−2686.
(20) Fulmer, G. R.; Miller, A. J. M.; Sherden, N. H.; Gottlieb, H. E.; Nudelman, A.; Stoltz, B. M.; Bercaw, J. E.; Goldberg, K. I. NMR Chemical Shifts of Trace Impurities: Common Laboratory Solvents, Organics, and Gases in Deuterated Solvents Relevant to the Organometallic Chemist. *Organometallics* **2010**, *29* (9), 2176−2179.
(21) *CrysAlisPRO, Ver. 171.36.20*; Agilent Technologies: Yarnton, Oxfordshire, England, 2011.
(22) Burla, M. C.; Caliandro, R.; Camalli, M.; Carrozzini, B.; Cascarano, G. L.; De Caro, L.; Giacovazzo, C.; Polidori, G.; Siliqi, D.; Spagna, R. IL MILIONE: A Suite of Computer Programs for Crystal Structure Solution of Proteins. *J. Appl. Crystallogr.* **2007**, *40* (3), 609−613.
(23) *Crystal Structure 4.2.2: Crystal Structure Analysis Package*; Rigaku Corporation: Tokyo 196-8666. Japan.
(24) Dolomanov, O. V.; Bourhis, L. J.; Gildea, R. J.; Howard, J. A. K.; Puschmann, H. OLEX2: A Complete Structure Solution, Refinement and Analysis Program. *J. Appl. Crystallogr.* **2009**, *42* (2), 339−341.
(25) Sheldrick, G. M. Crystal Structure Refinement with SHELXL. *Acta Crystallogr., Sect. C: Struct. Chem.* **2015**, *71*, 3−8.
(26) Bourhis, L. J.; Dolomanov, O. V.; Gildea, R. J.; Howard, J. A. K.; Puschmann, H. The Anatomy of a Comprehensive Constrained, Restrained Refinement Program for the Modern Computing Environment - Olex2 Dissected. *Acta Crystallogr., Sect. A: Found. Adv.* **2015**, *71* (1), 59−75.
(27) Spencer Kimball, P. M. and the GDT. *GIMP 2.10.14 (GNU Image Manipulation Program)*; 2019.
(28) Kratzert, D.; Holstein, J. J.; Krossing, I. DSR: Enhanced Modelling and Refinement of Disordered Structures with SHELXL. *J. Appl. Crystallogr.* **2015**, *48*, 933−938.
(29) Kratzert, D.; Krossing, I. Recent Improvements in DSR. *J. Appl. Crystallogr.* **2018**, *51*, 928−934.
(30) Allen, F. H.; Johnson, O.; Shields, G. P.; Smith, B. R.; Towler, M. CIF applications. XV. enCIFer: a program for viewing, editing and visualising CIFs. *J. Appl. Crystallogr.* **2004**, *37*, 335−338.
(31) Llunell, M.; Casanova, D.; Cirera, J.; Alemany, P.; Alvarez, S. *SHAPE (2.1)*; Universitat de Barcelona: Barcelona, Spain, 2013.
(32) Macrae, C. F.; Sovago, I.; Cottrell, S. J.; Galek, P. T. A.; McCabe, P.; Pidcock, E.; Platings, M.; Shields, G. P.; Stevens, J. S.; Towler, M.; Wood, P. A. *Mercury 4.0*: From Visualization to Analysis, Design and Prediction. *J. Appl. Crystallogr.* **2020**, *53* (1), 226−235.
(33) Macrae, C. F.; Bruno, I. J.; Chisholm, J. A.; Edgington, P. R.; McCabe, P.; Pidcock, E.; Rodriguez-Monge, L.; Taylor, R.; van de Streek, J.; Wood, P. A. *Mercury CSD 2.0* − New Features for the Visualization and Investigation of Crystal Structures. *J. Appl. Crystallogr.* **2008**, *41* (2), 466−470.
(34) Macrae, C. F.; Edgington, P. R.; McCabe, P.; Pidcock, E.; Shields, G. P.; Taylor, R.; Towler, M.; van de Streek, J. *Mercury*: Visualization and Analysis of Crystal Structures. *J. Appl. Crystallogr.* **2006**, *39* (3), 453−457.
(35) Bruno, I. J.; Cole, J. C.; Edgington, P. R.; Kessler, M.; Macrae, C. F.; McCabe, P.; Pearson, J.; Taylor, R. New Software for Searching the Cambridge Structural Database and Visualizing Crystal Structures. *Acta Crystallogr., Sect. B: Struct. Sci.* **2002**, *58* (3), 389−397.
(36) Taylor, R.; Macrae, C. F. Rules Governing the Crystal Packing of Mono-and Dialcohols. *Acta Crystallogr., Sect. B: Struct. Sci.* **2001**, *57* (6), 815−827.
(37) Parr, R. G.; Yang, W. *Density-Functional Theory of Atoms and Molecules*; Oxford University Press: New York, 1989.
(38) van Lenthe, E.; Baerends, E. J.; Snijders, J. G. Relativistic Regular Two-Component Hamiltonians. *J. Chem. Phys.* **1993**, *99*, 4597−4610.
(39) van Wüllen, C. Molecular Density Functional Calculations in the Regular Relativistic Approximation: Method, Application to Coinage Metal Diatomics, Hydrides, Fluorides and Chlorides, and Comparison with First-Order Relativistic Calculations. *J. Chem. Phys.* **1998**, *109* (2), 392−399.
(40) Pantazis, D. A.; Neese, F. All-Electron Scalar Relativistic Basis Sets for the Lanthanides. *J. Chem. Theory Comput.* **2009**, *5* (9), 2229−2238.
(41) Pantazis, D. A.; Neese, F. All-electron scalar relativistic basis sets for the actinides. *J. Chem. Theory Comput.* **2011**, *7* (3), 677−684.
(42) Pantazis, D. A.; Chen, X. Y.; Landis, C. R.; Neese, F. All-Electron Scalar Relativistic Basis Sets for Third-Row Transition Metal Atoms. *J. Chem. Theory Comput.* **2008**, *4* (6), 908−919.
(43) Zhao, Y.; Truhlar, D. G. A New Local Density Functional for Main-Group Thermochemistry, Transition Metal Bonding, Thermochemical Kinetics, and Noncovalent Interactions. *J. Chem. Phys.* **2006**, *125* (19), 194101.
(44) Klamt, A.; Schüürmann, G. COSMO: A New Approach to Dielectric Screening in Solvents with Explicit Expressions for the Screening Energy and Its Gradient. *J. Chem. Soc., Perkin Trans. 2* **1993**, No. 5, 799−805.
(45) Neese, F. An Improvement of the Resolution of the Identity Approximation for the Formation of the Coulomb Matrix. *J. Comput. Chem.* **2003**, *24* (14), 1740−1747.
(46) Kaneko, M.; Miyashita, S.; Nakashima, S. Bonding Study on the Chemical Separation of Am(III) from Eu(III) by S-, N-, and O-Donor Ligands by Means of All-Electron ZORA-DFT Calculation. *Inorg. Chem.* **2015**, *54* (14), 7103−7109.
(47) Neese, F. The ORCA Program System. *Wiley Interdiscip. Rev.: Comput. Mol. Sci.* **2012**, *2* (1), 73−78.
(48) Glendening, E. D.; Badenhoop, J. K.; Reed, A. E.; Carpenter, J. E.; Bohmann, J. A.; Morales, C. M.; Landis, C. R.; Weinhold, F. *NBO 6.0*; Theoretical Chemistry Institute, University of Wisconsin-Madison: Madison, WI, 2013.

https://dx.doi.org/10.1021/acs.inorgchem.0c03405
Inorg. Chem. 2021, 60, 2477−2491

(49) Kawasaki, T.; Okumura, S.; Sasaki, Y.; Ikeda, Y. Crystal Structures of Ln(III) (Ln = La, Pr, Nd, Sm, Eu, and Gd) Complexes with *N,N,N′,N′*-Tetraethyldiglycolamide Associated with Homoleptic $[Ln(NO_3)_6)]^{3-}$. *Bull. Chem. Soc. Jpn.* **2014**, *87* (2), 294−300.
(50) Nicolò, F.; Plancherel, D.; Bünzli, J. C. G.; Chapuis, G. Glasslike Structure in Crystalline Macrocyclic Complexes: Synthesis, X-Ray Diffraction, and Laser-Spectroscopic Investigation of Neodymium(III) and Europium(III) Complexes with 4,13-Dimethyl-1,7,10,16-Tetraoxa-4,13-Diazacyclooctadecane. *Inorg. Chem.* **1988**, *27* (20), 3518−3526.
(51) Boubals, N.; Wager, C.; Dumas, T.; Chanéac, L.; Manie, G.; Kaufholz, P.; Maire, C.; Panak, P. J.; Modolo, G.; Geist, A.; Guilbaud, P. Complexation of actinide(III) and lanthanide(III) with H_4TPAEN for a separation of americium fomr curium and lanthanides. *Inorg. Chem.* **2017**, *56* (14), 7861−7869.
(52) Cremer, D.; Kraka, E. A Description of the Chemical Bond in Terms of Local Properties of Electron Density and Energy. *Croat. Chem. Acta* **1984**, *57* (6), 1259−1281.
(53) Mayer, I. Charge, bond order and valence in the AB initio SCF theory. *Chem. Phys. Lett.* **1983**, *97* (3), 270−274.
(54) Mayer, I. Bond Order and Valence Indices: A Personal Account. *J. Comput. Chem.* **2007**, *28* (1), 204−221.
(55) Bridgeman, A. J.; Cavigliasso, G.; Ireland, L. R.; Rothery, J. The Mayer Bond Order as a Tool in Inorganic Chemistry. *Dalton Trans.* **2001**, No. 14, 2095−2108.
(56) Mulliken, R. S. Electronic Population Analysis on LCAO-MO Molecular Wave Functions. I. *J. Chem. Phys.* **1955**, *23* (10), 1833−1840.
(57) Reed, A. E.; Weinstock, R. B.; Weinhold, F. Natural population analysis. *J. Chem. Phys.* **1985**, *83* (2), 735−746.
(58) Davies, C. W. The extent of dissociation of salts in water. Part VIII. An equation for the mean ionic activity coefficient of an electrolyte in water, and a revision of the dissociation constants of some sulphates. *J. Chem. Soc.* **1938**, *0*, 2093−2098.
(59) Breen, P. J.; Horrocks, W. W., Jr Europium(III) luminescence excitation spectroscopy. Inner-sphere complexation of europium(III) by chloride, thiocyanate, and nitrate ions. *Inorg. Chem.* **1983**, *22* (3), 536−540.
(60) Zalupski, P. R.; Grimes, T. S.; Heathman, C. R.; Peterman, D. R. Optical absorption characteristics for $^7F_{0'} \rightarrow {}^4L_{6'}$ and $^7F_{0'} \rightarrow {}^7F_{6'}$ transitions of trivalent americium ion in aqueous electrolytemixtures. *Appl. Spectrosc.* **2017**, *71* (12), 2608−2615.
(61) Grimme, S. Semiempirical hybrid density functional with perturbative second-order correlation. *J. Chem. Phys.* **2006**, *124* (3), 034108.
(62) Kaneko, M.; Watanabe, M.; Matsumura, T. The Separation Mechanism of Am(III) from Eu(III) by Diglycolamide and Nitrilotriacetamide Extraction Reagents Using DFT Calculations. *Dalton Trans.* **2016**, *45* (43), 17530−17537.
(63) Basch, H.; Robin, M. B.; Kuebler, N. A. Electronic Spectra of Isoelectronic Amides, Acids, and Acyl Fluorides. *J. Chem. Phys.* **1968**, *49* (11), 5007.
(64) da Silva, V. H. M.; Quattrociocchi, D. G. S.; Stoyanov, S. R.; Carneiro, J. W. M.; da Costa, L. M.; Ferreira, G. B. A DFT Study of the Interaction between $[Cd(H_2O)_3]^{2+}$ and Monodentate O-, N-, and S-Donor Ligands: Bond Interaction Analysis. *J. Mol. Model.* **2018**, *24* (1), 39.
(65) Petit, L.; Daul, C.; Adamo, C.; Maldivi, P. DFT Modeling of the Relative Affinity of Nitrogen Ligands for Trivalent f Elements: An Energetic Point of View. *New J. Chem.* **2007**, *31* (10), 1738−1745.
(66) Lemonnier, J. F.; Guénée, L.; Beuchat, C.; Wesolowski, T. A.; Mukherjee, P.; Waldeck, D. H.; Gogick, K. A.; Petoud, S.; Piguet, C. Optimizing Sensitization Processes in Dinuclear Luminescent Lanthanide Oligomers: Selection of Rigid Aromatic Spacers. *J. Am. Chem. Soc.* **2011**, *133* (40), 16219−16234.

https://dx.doi.org/10.1021/acs.inorgchem.0c03405
Inorg. Chem. 2021, 60, 2477−2491